Research Square

Preprints are preliminary reports that have not undergone peer review.
They should not be considered conclusive, used to inform clinical practice,
or referenced by the media as validated information.

Hidden Spin-Valley-Locking Extends Room Temperature Spin Lifetime in 2D Perovskite Semiconductors

David Mitzi

david.mitzi@duke.edu

Duke University https://orcid.org/0000-0001-5189-4612

Volker Blum

Duke University

Matthew Beard

National Renewable Energy Laboratory https://orcid.org/0000-0002-2711-1355

Yifan Dong

University of California, Riverside https://orcid.org/0000-0003-2912-3322

Rayan Chakraborty

Duke University https://orcid.org/0000-0003-2925-4373

Leo Romanetz

University of Colorado Boulder https://orcid.org/0000-0002-3390-1265

Kelsey Garden

University of Utah https://orcid.org/0000-0002-0867-0741

Jacob Shelton

National Renewable Energy Laboratory

Matthew Hautzinger

National Renewable Energy Laboratory

Article

Keywords:

Posted Date: April 20th, 2026

DOI: https://doi.org/10.21203/rs.3.rs-7530828/v1

License: This work is licensed under a Creative Commons Attribution 4.0 International License. Read Full License

Additional Declarations: There is **NO** Competing Interest.

Hidden Spin-Valley-Locking Extends Room Temperature Spin Lifetime in 2D Perovskite Semiconductors

Rayan Chakraborty,[1,#] Yifan Dong,[2,3,#] Jacob L. Shelton,[2] Kelsey Garden,[2] Leo Romanetz,[4] Matthew P. Hautzinger,[2] Matthew C. Beard,[2,*] Volker Blum,[1,5] David B. Mitzi[1,5,*]

[1]Thomas Lord Department of Mechanical Engineering and Materials Science, Duke University, Durham, North Carolina 27708, United States
[2]National Laboratory of the Rockies, Golden, Colorado 80401, United States
[3]Department of Chemistry, University of California, Riverside, Riverside, California 92507, United States
[4]Department of Chemistry, University of Colorado, Boulder, Colorado 80309, United States
[5]Department of Chemistry, Duke University. Durham, North Carolina 27708, United States

[#]Authors contributed equally

Abstract.

Room-temperature control of spin, coupled with charge and light, remains a long-standing challenge for next-generation spin-optoelectronic applications. Although inversion symmetry breaking offers one path for spin control in semiconductors, strong spin dephasing at higher temperatures remains a persistent challenge. While hidden spin polarization (HSP) without global symmetry breaking provides another promising material design strategy, robust spin stabilization from HSP is yet to be experimentally realized. Here, we demonstrate that 2D hybrid organic-inorganic perovskites can provide spin stabilization at room temperature via hidden spin valley locking. We utilized functional nonprimary ammonium cations (NPACs) that induce giant spin splitting in 2D layers with varying spin-orbit coupling (employing Sn vs Pb) and enhanced dielectric screening, thereby restricting spin relaxation processes. Time-resolved experiments demonstrate optically generated spin-polarized carriers that persist for over *four nanoseconds at room temperature* without requiring an external magnetic field. Our design paradigm unlocks

inversion-symmetric semiconductors with ultralong spin lifetimes, broadening the materials options for light-driven spin control.

Introduction.

The efficient interconversion of spin, charge, and light in solution-deposited semiconductors promises advances in high-speed, low-power electronics, non-volatile memories, quantum sensing, computing, spin/optical interconnects, and other spin-optoelectronic applications.[1,2] In semiconductors, spin-polarized carriers are produced when circularly polarized light transfers angular momentum to charge carriers, which, however, may irreversibly lose their spin information through spontaneous spin-flipping and scattering processes as a result of interactions with the lattice and other carriers.[3,4] The scattering events collectively destabilize the spin-polarized state and thus decrease the associated spin lifetime τ_s. Lengthening τ_s in bulk semiconductors often requires cryogenic temperatures or an external magnetic field.[5,6] Room temperature measurements in inorganic semiconductors typically yields τ_s <100 ps, with larger values requiring complicated materials processing steps.[7-9] Developing materials with long τ_s will improve prospects for spin-optoelectronics, including applications such as spin-filters, spin light-emitting diodes, spin-transistors, spin photochemistry, and spin and light polarization detectors and sensors.[10-15]

The combination of spin-valley locking (SVL), persistent spin textures (PST), and screened electron-hole exchange interactions represents a key, though practically challenging to achieve, design target for extending τ_s in bulk semiconductors.[4,6,16,17] SVL is imposed on charge carriers present in spin-polarized electronic valleys (i.e., energy pockets in the momentum space). Consequently, the angular momenta of such carriers become efficiently protected, as a spin flip needs to be accompanied by a momentum transfer, which increases τ_s by making the overall dephasing process rare. On the other hand, PST preserves spin precession of mobile carriers by a

unidirectional internal effective magnetic field that results from spin-orbit coupling (SOC), ultimately restricting dephasing and increasing τ_s. The prospect of SVL with PST has prompted semiconductor discovery efforts focused primarily on breaking inversion symmetry.[17] Correspondingly, despite the prospects of inversion-symmetric bulk semiconductors for HSP-mediated spin control that were predicted over a decade ago,[18,19] little progress has been made. HSP is most frequently realized in 2D semiconductors such as transition metal dichalcogenides (TMDs).[20] Notably, in TMDs and at cryogenic temperatures (5 K), spin valleys in monolayers yield τ_s well over several nanoseconds; however, such polarizations disappear on a global scale (i.e., in bulk crystals) and prompt dephasing of spin.[16,21] Thus, although spin polarization driven by local inversion symmetry breaking has received recent attention,[20,22-27] experimental demonstrations of HSP in bulk systems primarily focus on introducing symmetry breaking through external perturbations, imposing restrictions on its ultimate practical usability. Recent work has shown that hybrid organic-inorganic semiconductors are a reliable platform for customizing spin-optoelectronic responses,[17,28-31] with a few exemplary cases of promising τ_s[32-34] and local spintronic effects.[25,35-37] Among strategies for structure-property tuning,[38-40] NPACs in 2D hybrid perovskite natural quantum well structures (Figure 1a) have recently been highlighted as a pathway for local symmetry breaking and SVL.[27]

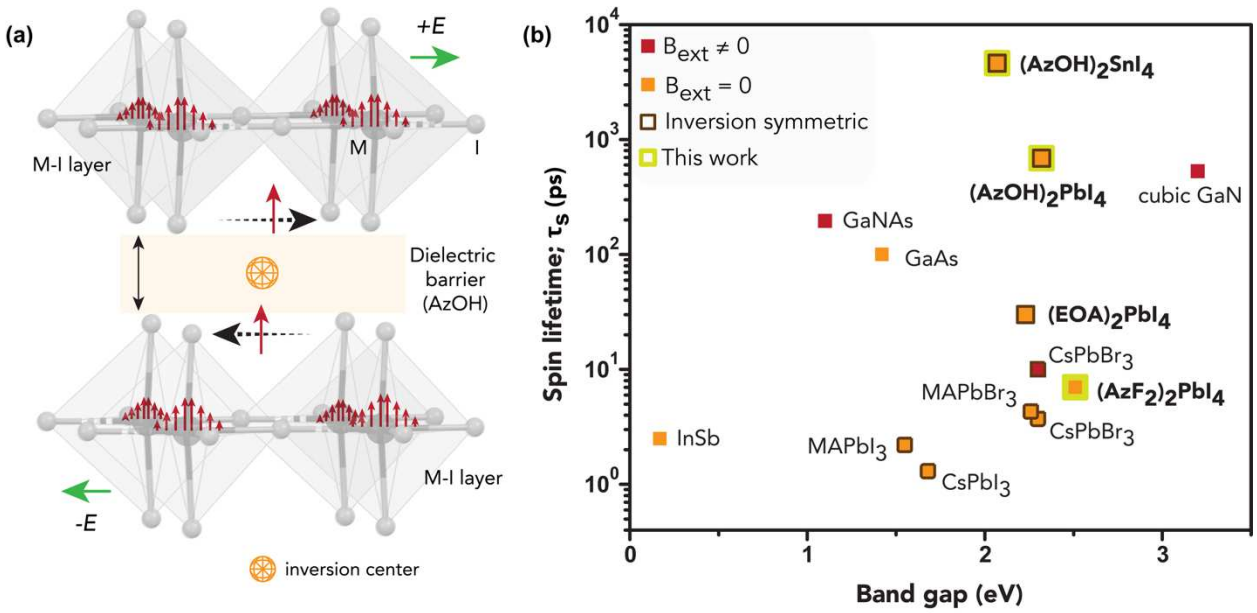


Figure 1. Spin lifetime in semiconductors. (a) Schematic showing stabilization of spin-polarized carrier wave packets (red arrows) due to HSP in the 2D metal halide layers of $(AzOH)_2MI_4$ (where M = Pb, Sn, and AzOH = 3-hydroxyazetidinium); black dashed arrows indicate their propagation directions following a semiclassical representation; +/-*E* refer to opposite electrical polarizations originating from asymmetric displacement of M and I atoms in the 2D layers. (b) Comparison of spin lifetime at (or near) room temperature among several semiconductors; the y-axis is plotted on a logarithmic scale; B_{ext} refers to an external magnetic field. The data points are collected from this work and literature references;[4,8,9,41-43] the data point for $(EOA)_2PbI_4$ was remeasured as part of the current study to provide consistency with azetidinium-based composition measurements.

In this work, we utilize compact NPACs based on an azetidinium backbone, for which the appended functional groups can induce symmetry-breaking distortions within the inorganic layer[44,45] and also increase the dielectric constant of the organic sublattice.[46,47] Effectively, our work combines two cation (A) functionalization approaches, targeting extended τ_s values in A_2PbI_4-related systems by: a) forming deep spin-valleys with nearly uniform spin texture at the conduction band (CB) to decrease the spin flipping and decoherence, and b) introducing a dielectric barrier through organic functionalization to screen carrier-lattice(carrier) interactions. As an outcome of the above targets, we identify a *globally inversion-symmetric structure* displaying long τ_s, wherein individual layer-dependent SVL becomes sufficient to preserve spin orientation

and angular momentum, leading to τ_s of >600 ps *at room temperature*. We extend the strategy to a Pb-free A_2SnI_4 composition with a reduced SOC strength (owing to Sn's lower atomic number than Pb)[3] and enhanced electrical polarization,[48] further elongating τ_s at room temperature, approaching five nanoseconds. Our results (Figure 1b) appear consistent with first-principles-computed spin-electronic structure and indicate examples for which local spin polarization can be effectively utilized in globally centrosymmetric materials, even in the absence of an external field, to extend τ_s beyond the typically achieved limits in bulk semiconductors.

Spin-Valley forms via Organic-to-Inorganic Symmetry Transfer.

2DHPs consist of a periodic arrangement of organic and inorganic layers held together through noncovalent N – H···I interactions at the organic-inorganic interface. Additionally, the noncovalent interactions among the organic molecules (A···A) provide rigidity to the organic sublattice and control the relative orientations of the N–H···I interactions. In turn, the interactions induce distortions in the 2D M–I layer and govern its symmetry. While primary ammonium cations (bearing -NH_3^+ groups) comprise the majority of reported 2DHP compositions, NPACs offer an effective pathway for introducing symmetry-breaking distortions.[27,44,45] Essentially, a primary ammonium group is more isotropic than a nonprimary ammonium. The latter typically implies sterically constrained and fewer N–H bonds (Figure 2a), consistent with less effective accommodation of strain in different directions in the latter case, leading to more distorted atomic arrangements.

Functionalized cyclic NPACs based on the azetidinium backbone (e.g., 3,3-difluoroazetidinium, AzF_2, and 3-hydroxyazetidinium, AzOH; Figure 2a) can enable novel intermolecular interactions. We find that AzF_2 crystallizes a 2DHP, $(AzF_2)_2PbI_4$ (Figure 2b), in the inversion-asymmetric *Pc* space group at room temperature (the structure was determined by single

crystal X-ray diffraction (SCXRD) measurements; see Methods for synthesis and measurement details and Table S1 in Supplementary Information (SI) for refinement parameters), which incorporates an asymmetric distribution of the N–H···I noncovalent bonds (Extended Data Figure 1). $(AzF_2)_2PbI_4$ exemplifies most inversion-symmetry-broken 2DHPs with Pb-I octahedral rotations (Figure 2d).[49] The Pb-I layer distortion is also evident from the differing bond lengths and angles (see Tables S2 and S3 in SI), showing the impact of variable N – H ···I interactions on the different vertices of the PbI_6 octahedra. The distortions shift the Pb atoms from the ideal octahedron center (< 0.1 Å), breaking the inversion symmetry of the 2D layer.

We synthesized another 2DHP with 3-hydroxyazetidinium (AzOH), which is a NPAC with a hydroxy substitution (see Methods for details). SCXRD measurements indicate that $(AzOH)_2PbI_4$ crystallizes in the centrosymmetric $P2_1/m$ space group, with inversion-asymmetric Pb–I layers (Figure 2c; Table S4 in SI). Compared to $(AzF_2)_2PbI_4$, a) the Pb–I–Pb bonds in $(AzOH)_2PbI_4$ distort with a less apparent octahedral rotation (Figure 2e); the distortion generates two distinct angles (177.2° and 164.2°), indicating anisotropic strain on the Pb–I layer, and b) the smaller deviation of the Pb–I–Pb angles from 180° and larger displacement of the Pb atoms from their octahedral center (0.16 Å) indicate a more effective overlap of the Pb and I orbitals[50] and larger polar distortion in $(AzOH)_2PbI_4$, respectively. The former leads to a smaller electronic gap, evidenced by the darker color of the crystals (Figure 2b). At the same time, the latter may significantly impact the spin polarization of the layer-localized charge carriers.[17] The atomic displacement in the Pb–I layers of $(AzOH)_2PbI_4$ resembles in-plane distortions in three-dimensional ferroelectrics like $PbTiO_3$ (Figure S1 in SI), and is the first such structure experimentally observed in 2DHPs (the dynamical stability of the distortion in the structure is

confirmed by phonon dispersion from first-principles simulations[51,52]; see Figure S2 in SI and Methods). [27]

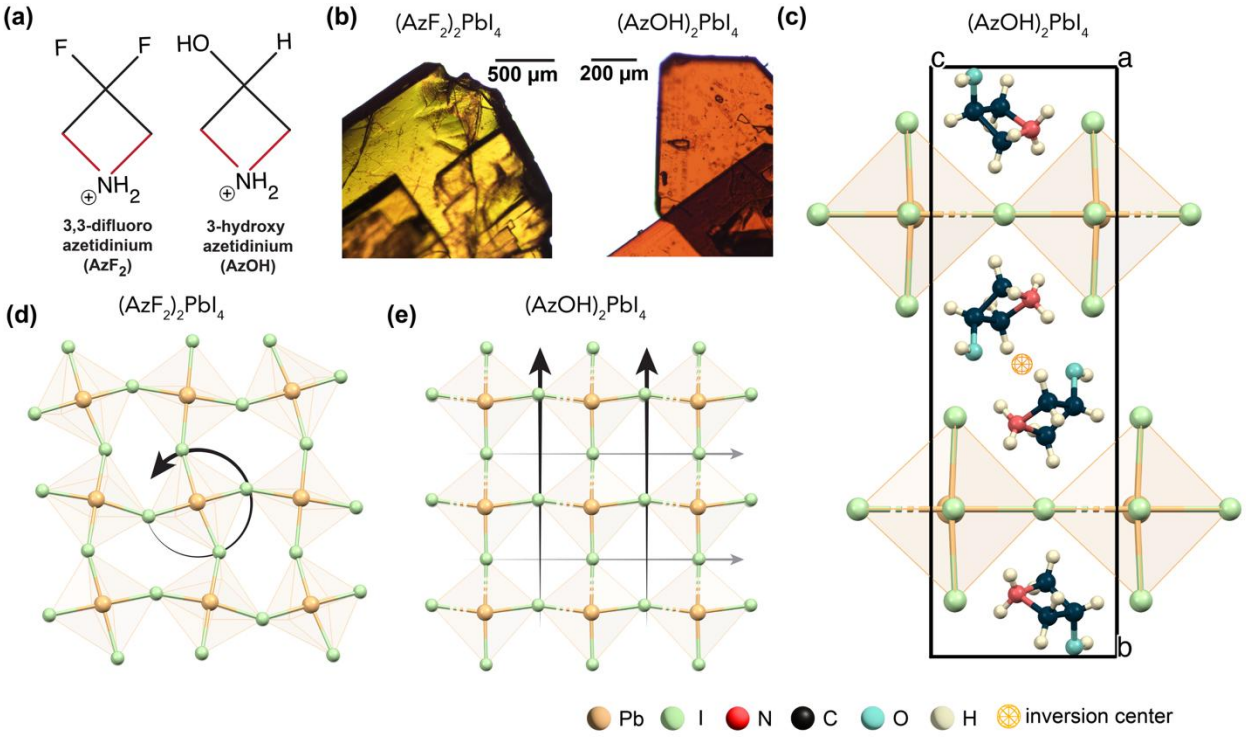


Figure 2. Hybrid azetidinium-based lead iodides.

(a) Structures of 3,3-difluoroazetidinium (AzF_2) and 3-hydroxyazetidinium (AzOH) cations, highlighting the N–C bonds (colored in red); (b) images of the corresponding 2DHP crystals; (c) crystal structure of $(AzOH)_2PbI_4$ at room temperature, obtained from X-ray diffraction; (d, e) distortion modes in the symmetry-broken Pb–I layers (the arrows indicate the relative displacements of the Pb-I-Pb angles).

In periodic solids, time-reversal and inversion symmetry cause the double degeneracy of electronic states for any crystal momentum $\boldsymbol{k}$. In 2DHPs, such as $(AzF_2)_2PbI_4$ and $(AzOH)_2PbI_4$, the CB and valence band (VB) edges are constructed by Pb and I orbitals that experience relativistic SOC (Figures 3a-b). The polar distortions in the Pb–I layers break the inversion symmetry and induce a $\boldsymbol{k}$-dependent energy split ($\Delta E^{\pm}$) of the bands into non-degenerate spin-

bands with spin expectation values. These values can be derived directly from the effective single-particle eigenvectors obtained from density functional theory (DFT).[40] Also, as they are shaped by large terms of the Hamiltonian (kinetic energy operator, symmetry of the external and electrostatic potential), they provide a reliable basis for the prediction of spin observables, unlike, for example, the quantitative prediction of a fundamental band gap, which is heavily impacted by the much more subtle details of the exchange-correlation energy expression.

Compared to the inversion-asymmetry in $(AzF_2)_2PbI_4$, which can lift the spin degeneracy in the unit cell, the inversion-symmetry in $(AzOH)_2PbI_4$ cancels polar distortions (see Figure 1a), preventing global spin polarization.[18] In $(AzF_2)_2PbI_4$, we observe a modest $\Delta E_{CB}^{\pm}$ of 14 meV at the CB in the first-principles calculations (Figure 3a; see Methods for details; briefly, hybrid HSE06 functional and SOC is used for the DFT simulation on a unit cell with 348 atoms; the complete band structure is provided in Figure S3 in SI; Extended Data Table 1 provides an extended list of the $\Delta E^{\pm}$ values), leading to a shallow spin-valley with uniform spin polarization (Figure S4 in SI), in agreement with similar 2DHPs with comparable structural asymmetry.[45,49] In $(AzOH)_2PbI_4$, larger distortions on the Pb – I layers cause prominent band splitting (Figure 3b; see Methods and Figure S5 in SI), creating sizable gaps between the spin sub-bands at the CB edge ($\Delta E_{CB}^{\pm} = 434\ meV$ and $\alpha_{CB} = 224.4\ meV.nm$; α is the spin-orbit coupling parameter, following a **k.p** representation of the energy bands[53]); a still substantial splitting is also observed at the VB edge ($\Delta E_{VB}^{\pm}$ =187 meV). The splitting introduces a larger offset for the lowest energy spin valleys at the CB ($\Delta k_{CB} = 0.78\ nm^{-1}$) compared to the VB ($\Delta k_{VB} = 0.07\ nm^{-1}$), leading to a pseudo-direct band gap between VB and CB edges. Notably, the $\Delta E_{CB}^{\pm}$ and α_{CB} magnitudes found in $(AzOH)_2PbI_4$ are comparable to previously explored noncentrosymmetric semiconductors with giant spin splitting—e.g., $(I\text{-}(CH_3)_3\text{-}NH_2)_2PbI_4$ and BiTeI—indicative of a strong SOC effect in the

presence of polar distortions.[45,54,55] Unlike the abovementioned semiconductors, in $(AzOH)_2PbI_4$, only the monolayers are inversion-asymmetric (Table 1), leading to HSP with spin-layer-locking, or hidden spin-valleys at the CB (Figure 3c and Figure S6 in SI). Effectively, in bulk $(AzOH)_2PbI_4$, the spin-polarized photoexcited electrons are not only valley polarized but also carry layer pseudospin, and opposite spins reside in adjacent layers at a defined linear momentum.[56] At these valleys, the spin polarizations become uniformly oriented along the direction normal to the 2D layers, *x* (Figure 3c), resulting in an effective helical periodicity ($l_H = \pi/\Delta k$) of 4.0 nm.[17,57] The large separation of the CB valleys in the momentum space may restrict intervalley scattering for the electron angular momentum and lead to suppression of τ_s.

In contrast to TMDs with a narrow van der Waals gap, the inorganic layers are separated by a barrier of AzOH molecules in $(AzOH)_2PbI_4$, which may lead to a more efficient real-space separation of the opposite spin-polarized CB valleys (Figure 1a). However, such localization is significantly weaker for the VB states, owing to the short interlayer distance between the out-of-plane iodine atoms (Extended Data Figure 2), which may facilitate fast dephasing of the spin-polarized photoexcited holes. In addition, the polar -OH group on the AzOH is expected to increase the dielectric constant of the organic barrier.[58] Consequently, there is reduced dielectric confinement in the 2D layers, leading to increased screening of carrier-carrier (lattice) interactions, which should produce enhanced charge carrier and spin lifetimes.[46,59-61] An analogous strategy was previously explored in $(EOA)_2PbI_4$ (Figure S7 in SI; EOA = 2-hydroxyethylammonium; HO-$(CH_2)_2$-NH_3^+), which showed a modest increase in τ_s that exceeded most previously reported 2DHPs.[43,47] A comparison of the dynamical changes in noncovalent interactions for $(EOA)_2PbI_4$ and $(AzOH)_2PbI_4$ using ab-initio molecular dynamics (AIMD) simulations (Extended Data Figure 3 and Supporting Note in SI) indicates that the restricted movement of the nonprimary ammonium

group leads to the observed structural asymmetry in $(AzOH)_2PbI_4$, which ultimately introduces the novel functionality of layer-dependent SVL.

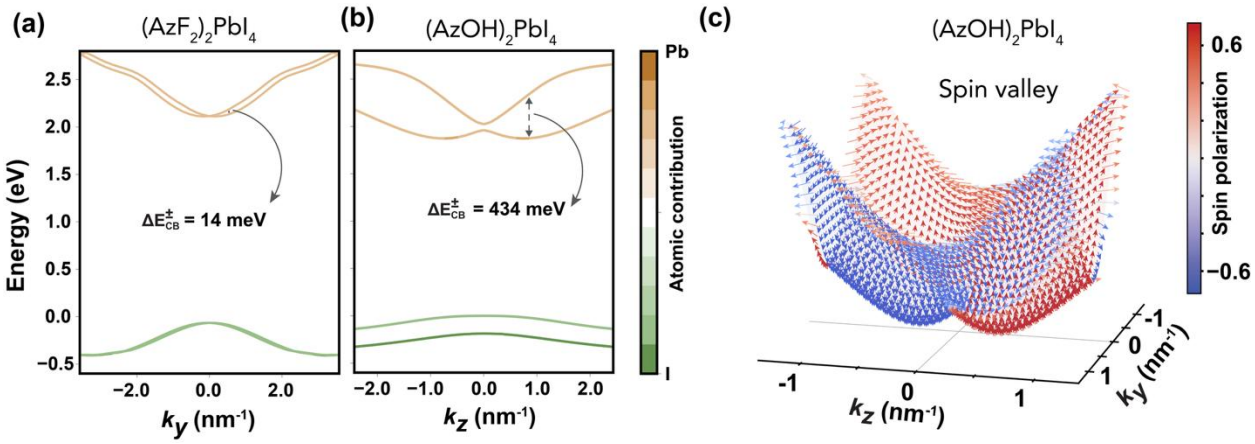


Figure 3. Spin Splitting in the azetidinium-based lead iodides.
(a, b) Electronic structures of the Pb and I-derived valence and conduction band edges for $(AzF_2)_2PbI_4$ and $(AzOH)_2PbI_4$ (computed with hybrid HSE06 functional in DFT with SOC); (c) spin texture at the conduction band minima of $(AzOH)_2PbI_4$ (computed with PBE functional in DFT and SOC); for $(AzOH)_2PbI_4$, one set of electronic bands and spin valley is shown, which corresponds to localized electronic states on one layer, although another set of degenerate states with opposite spin polarization exists (see Figure S5 in SI)

Table 1: Comparison of inversion symmetries and spin lifetimes (τ_s) at room temperature in the 2DHP compositions explored in this work. "+" and "-" refer to the presence and absence of the symmetry element, respectively, in the various local subunits of the structures. The space groups listed refer to those for the global structure. τ_s are measured through time-resolved circular dichroism (TRCD) on films (an extended list appears in Extended Data Table 2).

Composition	Inversion type			Space group	τ_s
	Octahedron	Intra-layer	Inter-layer		(ps)
$(EOA)_2PbI_4$	+	+	+	$P2_1/a$	30 ± 4.6
$(AzOH)_2PbI_4$	-	-	+	$P2_1/m$	686 ± 92

$(AzOH)_2SnI_4$	-	-	+	$P2_1/m$	4660 ± 830
$(AzF_2)_2PbI_4$	-	-	-	Pc	7 ± 1.5

Temperature-Dependent Spin Lifetime.

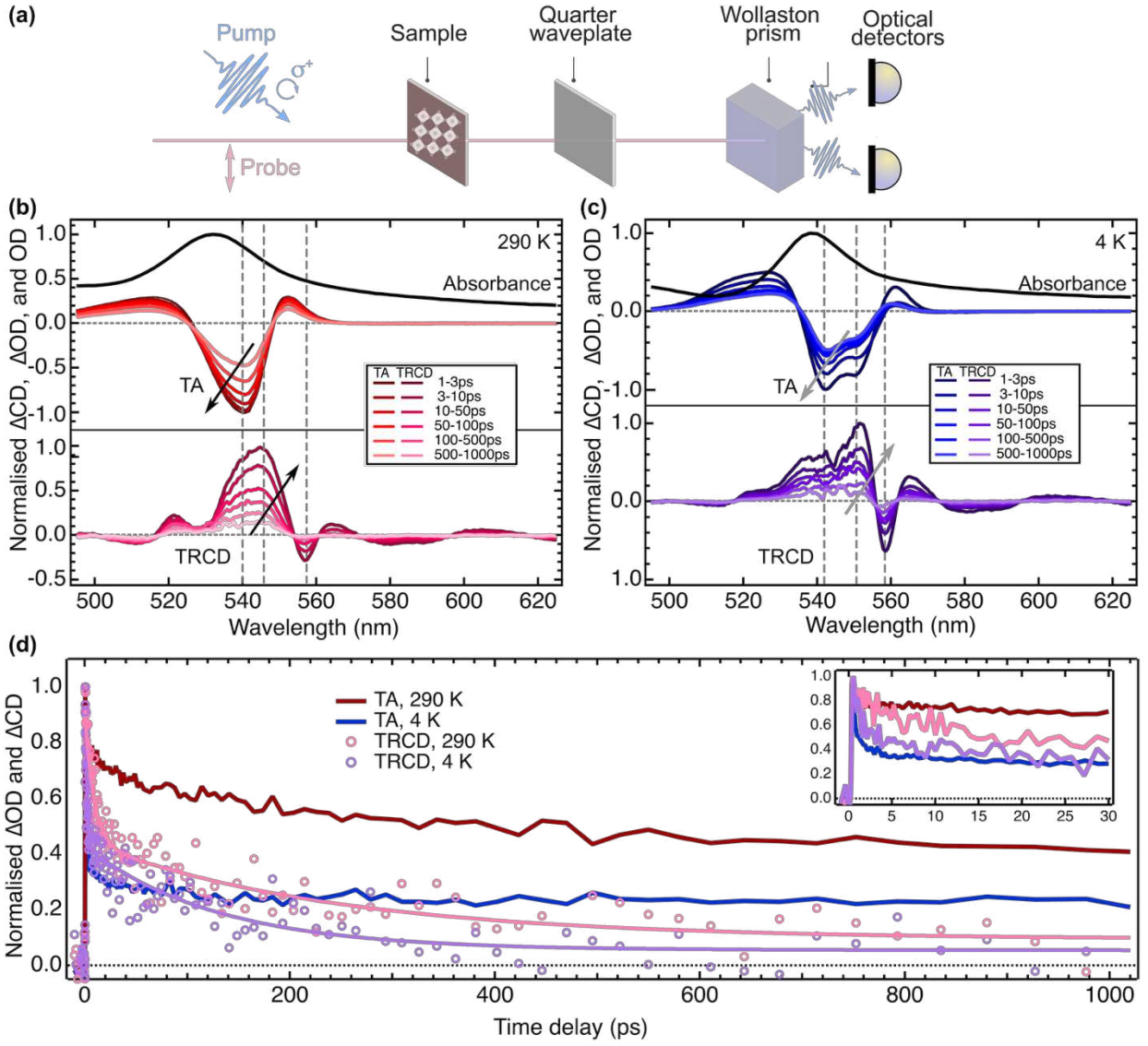


Figure 4. Spin and carrier lifetimes of $(AzOH)_2PbI_4$.
(a) Schematic for the transient absorption (TA) and time-resolved circular dichroism (TRCD) set up; the sum and difference of the signals from the optical detectors provide the TA and TRCD responses, respectively; (b) TA and TRCD spectra as a function of time delay along with the linear absorbance for $(AzOH)_2PbI_4$ thin films at (b) 290 K and (c) 4 K; the arrows indicate increasing

delay time; (d) normalized TA and TRCD kinetics extracted at the peak of the TRCD/TA (GSB maxima) spectra for carrier and spin lifetimes at 290 K and 4 K measured up to 1 ns; the inset shows the same kinetics for the first 30 ps of the measurement time window; the pump wavelength is at 485 nm with a repetition rate of 500 Hz and a fluence of 12 uJ/cm^2.

We next turned to time-resolved circular dichroism (TRCD)[62] and transient absorption (TA) measurements to study how the computed structural and electronic properties impact correlated carrier and spin dynamics of photogenerated carriers in the above set of 2DHPs (Table 1;see Methods). In the TRCD measurements, a circularly polarized pump at 485 nm carrying angular momentum of +1 or -1 was generated using a combination of a broadband linear polarizer and a quarter-waveplate. Under the angular momentum conservation rule, exciton states with well-defined angular momentum of $J_x = \pm 1$ are generated. After a time delay, a linearly polarized white light probe was sent to the sample, followed by a motorized quarter-waveplate and a Wollaston prism before being directed to two balanced broadband detectors (Figure 4a). The ellipticity imparted to the linearly polarized probe is analyzed to produce TRCD spectra and kinetics as a function of pump-probe delay and temperature.

The shallow spin-valley in $(AzF_2)_2PbI_4$ leads to a moderate τ_s at room temperature of 7 ps (Table 1 and Extended Data Figure 4; discussed below; Methods provide details on film deposition; powder X-ray diffraction measurements in Figure S8 in SI show characteristic Bragg peaks originating from vertically stacked 2D Pb-I layers on the substrate). In contrast, Figure 4b shows the normalized TA and TRCD kinetics along with the absorbance of $(AzOH)_2PbI_4$ films measured at 290 K. The observed ground state bleach (GSB) is centered at 540 nm and is red-shifted relative to the absorbance maxima. At 4 K, we observed a split in the GSB peak into two peaks centered at 542 nm and 550 nm. Compared to typical 2DHPs (e.g., phenethylammonium lead iodide), the longer carrier relaxation times of over one nanosecond in $(AzOH)_2PbI_4$ are consistent with the

design strategy that combines a large dielectric constant of the organic barrier and the intralayer electrical polarization, effectively protecting the carriers from interactions.[61] Turning to the TRCD spectra at 290 K and 4 K (bottom panels in Figures 4b and 4c), finer features can be observed compared to the TA spectra. The spin-oriented carriers induced by the pump pulse produce an effective magnetic field in the samples, underlying the induced CD spectra. The prominent photoinduced ΔCD absorption peaks match the GSB in the TA spectra at both temperatures, and all the features in the ΔCD spectra decay simultaneously, indicating they are simply tracking the spin-polarized carrier dynamics. To extract τ_s and gain insight into the spin relaxation mechanisms, we compared the normalized TRCD transients at 290 K and 4 K (Figure 4d). At 290 K, two decay components can be observed with the half lifetime components fitted as 8.1 ps and 343 ps (Extended Data Table 2; corresponding TA half lifetime components are 31.2 ps, and 668 ps). As the temperature decreases to 4 K, the average spin lifetime of $(AzOH)_2PbI_4$ becomes shorter, with the half lifetime almost a third of that at 290 K (the two half lifetime components were fitted to be 1.4 ps and 128 ps, respectively). SCXRD (Table S4 in SI) and temperature-dependent UV-vis spectra (Figure S9 in SI) do not suggest a phase transition, but likely an increase in excitonic contribution at lower temperatures (as evidenced by the marginal redshift of the absorption peak); we also observe negligible fluence dependence of the TA/TRCD dynamics at the probed temperatures (Extended Data Figure 5); therefore, the change in TRCD response with temperature can be solely attributed to spin dynamics. Among the two components, the shorter one likely corresponds to the fast depolarization of the photogenerated holes in the VB, consistent with weak localization (Extended Data Figure 2), and also prior reports of hybrid perovskites.[63] The TRCD measurements in reflectance mode for the single crystal (Extended Data Figure 6) show a comparable spin lifetime as the thin film, indicating intrinsic effects govern the measured spin

dynamics in $(AzOH)_2PbI_4$. The slightly shorter τ_s at lower temperatures indicates that momentum and spin-dependent scattering events do not significantly influence the room-temperature τ_s; instead, the lifetime is *likely* governed by the electron-hole exchange interactions, which increase at lower temperatures due to less thermal energy and more electron-hole interactions, consistent with the faster dynamics at earlier times in the TA kinetics at 4 K compared to the same at room temperature (inset of Figure 4d).[64,65] Comparing with the TA kinetics, we find that the average spin lifetime is shorter than the average carrier lifetime, indicating that the τ_s is not primarily limited by carrier recombination, consistent with prior reports.[47,61] To our knowledge, $(AzOH)_2PbI_4$ displays the longest τ_s (686 ps) among inversion-symmetric semiconductors—i.e., the value is comparable to or even longer than many noncentrosymmetric semiconductors at room temperature (Figure 1b).

Despite the similar functionalization and overall molecular shapes of AzOH and EOA, the difference between τ_s of $(EOA)_2PbI_4$ and $(AzOH)_2PbI_4$ (see Extended Data Figure 4) presumably results from their differences in symmetry elements. As EOA maintains inversion symmetry on the Pb-I layer, although circularly polarized light can transiently stabilize spin-polarized states, the carriers' angular momentum isn't protected due to spin degeneracy; stabilization can therefore easily be lost through spin flips, carrier-lattice interactions, and recombination, leading to a moderate τ_s of 30 ps. Unlike $(EOA)_2PbI_4$, AzOH introduces symmetry-breaking distortions and spin valleys in the Pb–I layer of $(AzOH)_2PbI_4$, where the offset of the band edges may delay the electron-hole recombination, allowing for different scattering pathways to impact spin dephasing. The above discussion points to specific structural distortions (e.g., to form SVL) and the choice of organic cation (e.g., to reduce dielectric confinement) as underlying causes of robust spin polarization in $(AzOH)_2PbI_4$.

Extension of the Materials Design Strategy.

Structural distortions in the 2D layers of 2DHPs result from noncovalent interactions, enabling their replication across compositions that preserve these interactions while offering differing optoelectronic responses. Since $(AzOH)_2PbI_4$ exhibits a long τ_s at room temperature through SVL, substituting Pb with Sn may preserve the polar distortion and reduce the SOC-induced scattering,[3] leading to further elongation. We synthesized $(AzOH)_2SnI_4$ (see Methods), which is isostructural to $(AzOH)_2PbI_4$ with slight deviations in the lattice parameters (evidenced by the SCXRD measurements; Figure 5a, and Table S6 in SI). The darker color of the resulting crystals compared to $(AzOH)_2PbI_4$ results from a smaller optical bandgap (Figure S10 in SI). The off-centering of the Sn atoms in $(AzOH)_2SnI_4$ by ~0.20 Å generates a polar distortion on the Sn-I plane, which is slightly larger than that in $(AzOH)_2PbI_4$. DFT calculations indicate that the minimum of the CB creates an offset from the VB maximum at the Γ-point, and forms spin valleys (Figure S11 in SI provides the complete band structure). Interestingly, DFT calculations show that shallow energetic valleys persist, even when SOC is not considered (Extended Data Figure 7), which aligns with previous findings in NPAC-based 2DHPs[45] and the idea that the asymmetric arrangement of metal-halide bonds around the Sn nuclei (an outcome of polar distortions) contributes to valley formation.[55] The SOC further splits the Sn-derived CB ($\Delta E_{CB}^{\pm} = 234\ meV,\ \alpha_{CB}$ = 213 meV.nm, and $\Delta k_{CB} = 0.71\ nm^{-1}$, following a **k.p** representation of the energy bands[53]) and induces spin-layer-locking. The spin textures on the k_y-k_z and k_x-k_z planes (Extended Data Figure 7) indicate a uniform out-of-plane spin polarization. While the $\Delta E_{CB}^{\pm}$ decreases by ~200 meV on substituting Pb in $(AzOH)_2PbI_4$ with Sn and a weaker SOC effect, the spin splitting parameters and the $\Delta E_{VB}^{\pm}$ remain comparable (Extended Data Table 1), consistent with the SOC-independent origin of the observed valleys at the band edges. The deeper valleys at the CB edge along the Γ – Z direction

suggest robust preservation of the angular momenta for the photoexcited electrons (Figure 5b) and better insulation of them from both intervalley and interlayer dephasing mechanisms, compared to the holes in the VB. Accordingly, the TRCD spectra (Figure 5c; Extended Data Table 2 and Figure S12 in SI list the fitting parameters and show spin dynamics as functions of probe wavelength, respectively) indicate a significantly long τ_s of ~4.7 ns in $(AzOH)_2SnI_4$ at room temperature (the corresponding TA measurements indicate carrier lifetimes of over 10 ns; Extended Data Figure 8). The reciprocity of the TRCD spectra on reversing the helicity of light is consistent with hidden SVL in $(AzOH)_2SnI_4$ (Figure 5d).

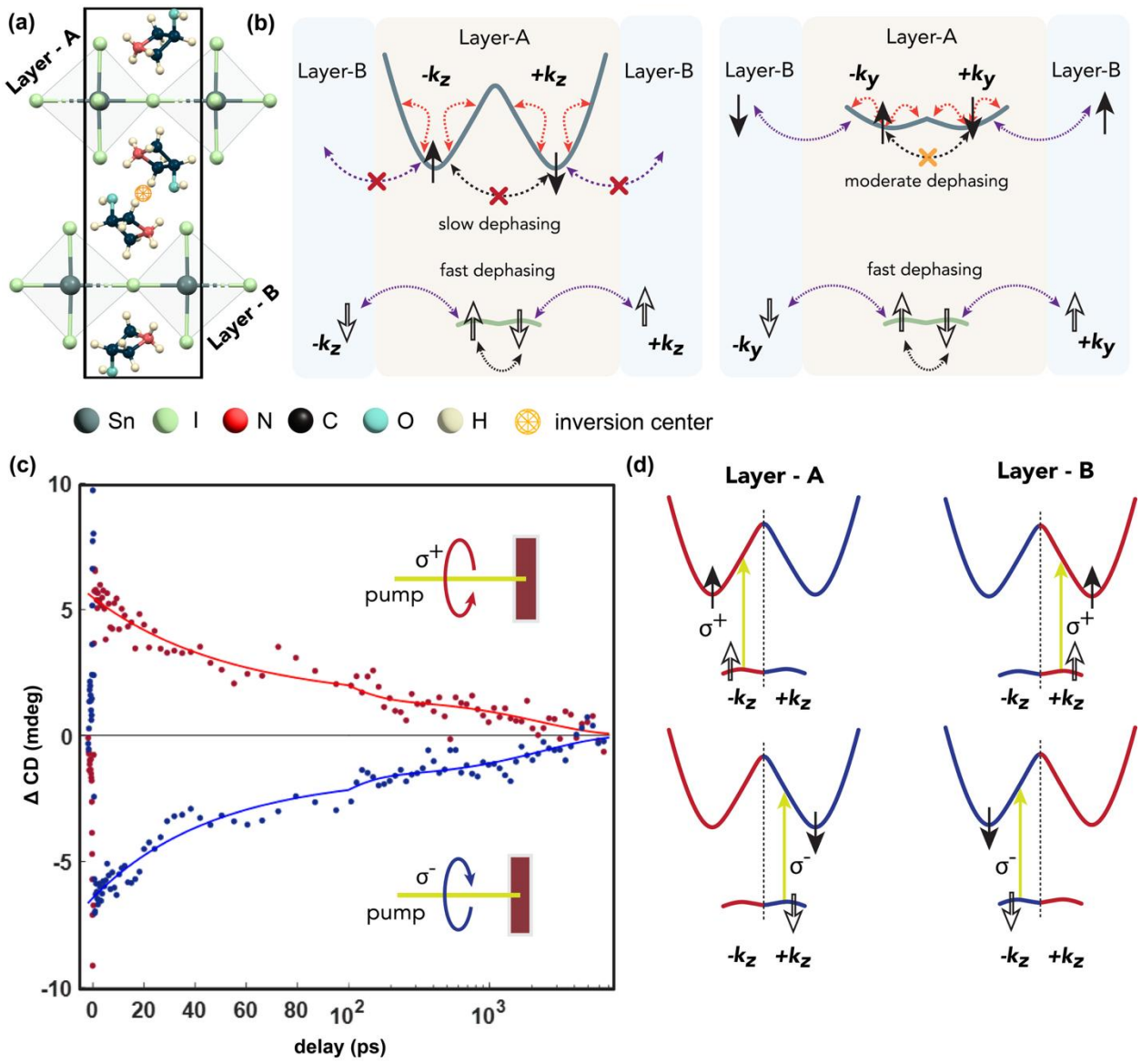


Figure 5. Spin dynamics of $(AzOH)_2SnI_4$ at room temperature.

(a) XRD-derived crystal structure of $(AzOH)_2SnI_4$ at room temperature; (b) schematics show possible scattering pathways (red, black, and purple dashed arrows for intravalley, intervalley, and interlayer scatterings, respectively) along two perpendicular directions (Γ-Z; left panel and Γ-Y; right panel) of the 2D layer plane for carrier angular momenta (***J***) in the AzOH-based compounds; up and down arrows indicate states with $+J_x$ and $-J_x$, respectively, while solid and hollow arrows indicate electron and hole-derived states, respectively; (c) comparison of TRCD response of $(AzOH)_2SnI_4$ film at 290 K on left (top panel) and right (bottom panel) circularly polarized excitation (pump) at different time delays where the pump wavelength is at 400 nm with a repetition rate of 500 Hz and a fluence of 62 μJ/cm^2; the data after 1 ps has been used for the fitting (solid lines) to mask the region dominated by the instrument response from the dynamics; (d) simplified schematics of the consequence of excitation on different layers of the unit cell.

As $(AzOH)_2SnI_4$ provides a reduced $\Delta E_{CB}^{\pm}$ but comparable Δk_{CB} (and comparable VB spin splitting parameters), inter-valley and inter-layer scatterings (Figure 5b) do not appear as the dominant factors behind the longer τ_s, compared to isostructural $(AzOH)_2PbI_4$. In addition to its intrinsic long carrier lifetime, the difference thus likely stems from the reduced SOC effect with Sn, which helps retain angular momenta for the photogenerated mobile electrons at the CB minimum and suppresses intra-valley scattering (orange arrows in Figure 5b). Additionally, the increased electrical polarization caused by the polar distortion in the latter may also better screen the electron-hole wavefunctions and help preserve the optically oriented angular momenta of the electrons due to the stronger local orbital moment.[33,55,66,67]

Comparison of τ_s across the semiconductor space explored in this work and existing literature (Figure 1b, Extended Data Table 2 and Figure 4, and Table S7 in SI) suggests that SVL is crucial for elongating τ_s at room temperature. Based on the observed trends in τ_s in this work, we propose that the dominant scattering pathways (Figure 5b) in the AzOH-based materials likely include a) intra- and inter-valley scatterings for photoexcited electrons, which may be restricted by the uniformity of the spin polarization, and the large required momentum transfer for spin flipping, respectively; b) inter-valley scattering for photoexcited holes; c) inter-layer dephasing, which may occur for both holes and electrons at the higher energy spin valley along Γ–Y dispersion (Extended Data Figure 2) due to the short inter-layer distance.

Conclusions.

While TMDs host spin valleys and display long τ_s at cryogenic temperatures, thermal instabilities lead to short room-temperature lifetimes (e.g., < 30 ps),[68] similar to III-V semiconductors.[69] Apart from semiconductors, semimetals such as WTe_2 have been demonstrated to display nanosecond-long τ_s at room temperature due to the exotic topologically protected states.[70] However, arduous

sample fabrication methods and/or external field requirements for enabling long optically-excited τ_s at room temperature have remained a critical hurdle. On the other hand, solution-processed hybrid perovskites also typically show short τ_s (e.g., < 5 ps without an external field).[4,36,43] In contrast to the above, the $(AzOH)_2MI_4$ systems are relatively straightforward to synthesize, while also displaying 0.6-4.7 ns (depending on choice of M and SOC strength) long τ_s without an external field at room temperature. The long lifetime of the excited states, as probed through TRCD, is consistent with the first-principles-computed spin-valley and the presence of valley-polarized electron-hole pairs.[71] *Crucially, our results suggest that the requirement of inversion symmetry breaking with SOC to lift the global spin degeneracy is unnecessary for extending τ_s, if within locally asymmetric structures, spin valleys can be formed, and interactions governing spin relaxations can be restricted.* As the structural asymmetry and restricted dynamics of the nonprimary ammonium group underlie such spin-valley formation and longer carrier lifetimes, compositions and fabrication strategies can be easily customized through material design approaches. For example, substituting Pb with Sn effectively weakens SOC-induced scattering while preserving the local polar distortion in the 2D layers of $(AzOH)_2MI_4$, further prolonging the spin lifetime. Measurements such as spin- and angle-resolved photoemission spectroscopy,[72] and circular photogalvanic effect measurements,[17] remain promising avenues to gain a deeper understanding of hidden spin valleys in 2DHPs. Therefore, we anticipate significant short-term progress with broader implications for spin-optoelectronic research, driven by hidden spin-valley physics and local symmetry breaking in 2DHP semiconductors.

Methods

Experimental methods.

Materials: Lead iodide (PbI_2, 99.99%, TCI Chemicals), tin iodide (SnI_2, 99.99%, Aldrich), hydroiodic acid solution (HI, 57 wt % in H_2O, stabilized, 99.95%, Sigma-Aldrich), hypophosphorus acid (H_3PO_2, 50 wt. % in H_2O, Aldrich), 3-hydroxyazetidine hydrochloride (AzOH.HCl, 95%, Enamine), 3,3-difluoro azetidine hydrochloride (AzF_2.HCl, 95%, Enamine), ethanolammonium iodide (EOAI, GreatCell), N,N-dimethyl formamide (DMF, Sigma-Aldrich, anhydrous, 99.8%), chlorobenzene (Sigma-Aldrich, anhydrous, 99.8%), and diethyl ether (> 99%, stabilized, VWR chemicals) were used as received.

Single crystals of $(AzF_2)_2PbI_4$, $(AzOH)_2PbI_4$ and $(AzOH)_2SnI_4$: For synthesizing $(AzF_2)_2PbI_4$ crystals, 1 mmol (130 mg) AzF_2.HCl and 0.5 mmol (230 mg) PbI_2 were sonicated in 2.3 ml HI at room temperature. The solution was placed on a refrigerator shelf, maintaining 2 ^{O}C for 24 hours. The precipitated yellow transparent crystals were filtered out, washed with diethyl ether, and used for further analyses. The large excess of I^- ions in the solution ensures negligible Cl^- incorporation from the cation salt in the resulting crystals.[73]

The $(AzOH)_2PbI_4$ crystals were synthesized by dissolving 0.5 mmol (231 mg) PbI_2 in 0.25 ml HI by heating in a water bath at 80 $^{\circ}$C. The clear yellow solution was subsequently cooled to room temperature. In a separate vial, one mmol (110 mg) AzOH.HCl was sonicated for 5 minutes in 0.25 ml HI at room temperature. These solutions were mixed in a glass vial and transferred to a refrigerator shelf, maintained at 2 $^{\circ}$C. After 24 hours, the precipitated red crystals were filtered out, washed with diethyl ether, and stored in an N_2-filled glove box.

The $(AzOH)_2SnI_4$ crystals were synthesized in a slightly modified way, during which 0.5 mmol SnI_2 was taken in a sealed tube (loaded under an N_2 atmosphere) to which a mixture of 0.4 ml HI and 0.1 ml H_3PO_2 was injected. The solution was heated in a water bath at 80 $^{\circ}$C for 30 minutes to ensure complete dissolution, then cooled to room temperature. Separately, 3 mmol

AzOH.HCl was dissolved in 0.6 ml HI at room temperature and injected into the sealed tube. The tube was then transferred to a refrigerator shelf, maintained at 2 °C. After 24 hours, the precipitated black-appearing crystals were filtered using a suction filter. The crystals were washed with diethyl ether, dried with N_2-flow, and then transferred into a N_2-filled glove box.

Thin film deposition: Thin films on glass or sapphire substrates were deposited by spin-coating. In an N_2-filled glove box, 0.25 mmol of $(AzOH)_2PbI_4$ or $(AzOH)_2SnI_4$ was dissolved in 0.5 ml DMF at room temperature by stirring for 30 minutes on a magnetic stirrer to prepare the precursor solutions. These solutions were then spin-coated in the same glovebox at 3000 rpm for 30 seconds onto the substrates. 100 μl chlorobenzene was dropped on the substrate 20 seconds into the spin cycle. The substrates were then annealed on a hot plate at 60 °C for two minutes. For the follow-up spectroscopic measurements, the films of $(AzOH)_2SnI_4$ were loaded onto an ultra-high-vacuum flange with UV-fused silica viewports, which was sealed with copper gaskets in the same glove box as for the film deposition. For depositing the $(AzF_2)_2PbI_4$ films, 0.2 mmol of $(AzF_2)_2PbI_4$ crystals were dissolved in 0.5 ml DMF, and the solution was spin-coated at 3000 rpm for 30 sec on the substrate. To prepare the films of EOA_2PbI_4, a 2:1 molar ratio of EOAI and PbI_2 was dissolved in DMF in an N_2-filled glovebox to form the precursor solution. The solution was then spin-coated at 3000 rpm for 30 seconds and annealed at 70 °C for 10 minutes.

Single-crystal X-ray diffraction: Single-crystal X-ray diffraction (SCXRD) data were collected using a Rigaku XtaLAB Synergy-S diffractometer using Mo Kα radiation (λ = 0.71073 Å). Data reduction and absorption correction were applied using CrysAlisPro. The structures were solved and refined using SHELXT intrinsic phasing and the SHELXL least-squares method as implemented in the Olex2 software package. All atomic positions were refined without restrictions on the atomic occupancy, and thermal parameters were refined anisotropically. Occupancy values

of all atoms were found to be 1 (with numerical errors of < 2%), consistent with the expected compositional formula for the hybrid lead iodide perovskites. Consequently, in the reported CIFs, the occupancy values were set as 1 with the numerical errors discarded. Average heteroatom bonding distances from the structure refinement also agree with the azetidinium cation assignment. For example, in the room-temperature data for $(AzF_2)_2PbI_4$, the average C-F distance (1.33 Å), agrees with literature values (e.g., 1.35 Å in 3,3-difluoroazetidinium bismuth chloride[74]). For $(AzOH)_2PbI_4$ and $(AzOH)_2SnI_4$, the average C-O distances (1.40 Å and 1.41 Å, respectively) also agree with expected values (1.40 Å for 3-Azetidinol[75]). For $(AzOH)_2PbI_4$ or $(AzOH)_2SnI_4$, the hydrogen atoms were identified from the difference peaks, and the atomic positions were refined afterward. For $(AzF_2)_2PbI_4$, the hydrogen atom positions were initially approximated based on adjacent atomic connectivity and were further refined afterward.

Powder X-ray diffraction: The powder X-ray diffraction (PXRD) measurements at room temperature were carried out on a PANalytical Empyrean Powder X-ray diffractometer using Cu Kα radiation (λ= 1.54 Å).

UV-vis measurements: The low-temperature UV-vis absorption measurements were performed using a modified setup, as described in reference [76]. Briefly, a closed-cycle helium Montana Instruments Cryostation conductively cooled the sample to 10 K. Intermediate temperatures were achieved with the installed stage heaters in the cryostat and measured with a sample thermometer mounted to the cold finger, where the sample was also mounted. The probe light was produced with a tungsten-halogen lamp coupled to a monochromator whose exit slit has been removed and output imaged onto an optical fiber. After the fiber, the probe was collimated and refocused onto the sample through two achromatic lenses with a long-pass filter to eliminate residual UV light from the lamp. Then the diverging lens after the sample was again recollimated

and refocused with another pair of achromatic lenses to an optical fiber. The optical fiber is connected to a NewFocus Model 2307 balanced photodiode (with a blocked reference input) whose signal was measured with a Zurich-Instruments UHFLI, 600 MHz bandwidth lock-in amplifier with DC coupling and a 0 Hz reference frequency. The light incident on the sample (I_0) was collected by measuring the lamp spectrum with all the cryostat optics in place and through a blank sapphire substrate at room temperature. The transmitted light intensity through the sample (I) and I_0 were both background subtracted with a dark spectrum that was collected with the probe blocked. The absorbance (OD) was measured as $-\log(I/I_0)$ at various set temperatures. The same I_0 spectrum was used for measuring absorbance at all temperatures.

Spin lifetime measurements: Time-resolved circular dichroism (TRCD) was used to measure the spin lifetimes of the perovskite thin films.[77] TRCD was carried out using a 1-kHz Ti:sapphire laser (Coherent Astrella, pulse width = 100 fs). One portion of the 800-nm fundamental beam was directed to an optical parametric amplifier (Quantronix Palitra Duo) to generate visible pump pulses, chopped at 500 Hz. The pump pulse was sent to a linear polarizer (Thorlabs) followed by a broadband quarter waveplate (Thorlabs) to yield a circularly polarized pump. Another portion of the 800-nm fundamental beam was directed to a sapphire plate to generate broadband white light probe pulses. The probe was sent through a linear polarizer and then focused onto the sample. The delay between the pump and probe pulses was varied using a mechanical delay stage, and the angle between the pump and probe beams was less than 10°. The pump-induced ellipticity of the probe polarization was recorded using a broadband quarter waveplate (Thorlabs) and a α-BBO Wollaston prism (Thorlabs). The s- and p-planes of the probe beam were split by the Wollaston prism and were directed to two balanced CMOS broadband detectors. The difference in the response of the two detectors is analyzed as the TRCD signal, while the sum corresponds to the

TA signal.[62] For the temperature-dependent TA measurements, the ground state bleach (GSB) peak position shifted with temperature. For the temperature-dependent TA measurements, the ground state bleach (GSB) peak position shifted with temperature. Extracting kinetics at a fixed probe energy across the different temperatures could distort the apparent kinetics. To address this, we followed a peak-tracking approach in our analysis, in which the actual GSB peak energy was identified at each temperature, and the corresponding kinetics were extracted at that corresponding energy. Specifically, the kinetics were extracted at 540 nm at 290 K and at 545 nm at 4 K. This analysis ensures that the observed shortening of the spin lifetime at low temperature is not an artifact of bandgap or absorption-coefficient shifts, nor of TRCD/TA amplitude changes unrelated to the kinetics.

Computational methods.

All first-principles density functional theory (DFT) simulations were performed using the all-electron, full-potential electronic structure code package FHI-aims.[51,78,79]

Structure optimization: For $(AzOH)_2PbI_4$ and $(AzOH)_2SnI_4$, a (2×2) lateral supercell (with respect to the underlying Pb (Sn) – I lattice, constituting two Pb (Sn) – I layers and four Pb (Sn) atoms in each layer) of 248 atoms was constructed from the room temperature SCXRD-derived structure by extending the atomic coordinates and lattice parameters in the *a* and *c* lattice directions. For $(EOA)_2PbI_4$, a (1×2) lateral supercell (with respect to the underlying Pb – I lattice, constituting one Pb – I layer and four Pb atoms in the layer) of 116 atoms was constructed from the room temperature crystal structure reported by Mercier and co-workers.[80] For $(AzF_2)_2PbI_4$, the experimentally obtained crystal structure with 348 atoms was used. The atomic coordinates of all atoms and the lattice parameters were optimized using the PBE+TS functional (Perdew-Burke-Ernzerhof (PBE) exchange correlation[81] with Tkatchenko-Scheffler (TS) dispersion correction[82]),

numerical atom-centered orbital (NAO) basis sets with FHI-aims "tight" numerical defaults, and *k*-point grids of (4 × 2 × 4), (4 × 2 × 4), (4 × 3 × 5), and (2 × 5 × 2) for $(AzOH)_2PbI_4$, $(AzOH)_2SnI_4$, $(EOA)_2PbI_4$, and $(AzF_2)_2PbI_4$, respectively. The optimized lattice parameters were found to have < 2.5% deviations from the SCXRD-derived structures. The optimized structures were re-oriented such that the metal halide layer stacking directions align with the crystallographic *a*-axis (see Figure 2c). All subsequent calculations were performed using these optimized structures. The optimized structures are provided in Section D of SI.

Electronic band structure and spin texture: The electronic band structure calculations were performed using the Heyd−Scuseria−Ernzerhof (HSE06) hybrid functional[83,84] with standard exchange mixing parameter 0.25 and screening parameter[85] 0.11 $Bohr^{-1}$ and second-variational non-self-consistent spin−orbit coupling (SOC).[79] FHI-aims "intermediate" numerical defaults and *k*-point grids of (3 × 4 × 4) were used for $(AzOH)_2PbI_4$ and $(AzOH)_2SnI_4$, and (3 × 5 × 3) was used for $(AzF2)_2PbI_4$. The spin textures were simulated using the PBE functional and with an extensively benchmarked second-variational, non-self-consistent approach for SOC.[79,86]

Phonon band structure: The phonon eigenvectors were computed on the optimized supercell of $(AzOH)_2PbI_4$ using the finite displacement method with a displacement value of 0.005 Å. FHI-aims with "tight" numerical defaults, and the PBE+TS scheme was used to compute the forces. The Phonopy package was used to generate the displaced structures and for further post-processing.[87]

Ab initio molecular dynamics: Ab initio molecular dynamics (AIMD) simulations were carried out with the optimized 2×2 lateral supercell containing 248 atoms ($(AzOH)_2PbI_4$) or 116 atoms ($(EOA)_2PbI_4$) using the FHI-aims "light" numerical defaults with PBE+TS functional. AIMD trajectories of 16.5 ps ($(AzOH)_2PbI_4$) or 16.2 ps ($(EOA)_2PbI_4$) in length with 0.75 femtoseconds

timestep were simulated within the constant-volume-temperature-thermostat (NVT) ensemble at T = 300 K. The Maxwell-Boltzmann distribution was used to initialize the atomic velocities corresponding to 300 K, following which the Bussi-Donadio-Parrinello stochastic velocity rescaling thermostat (relaxation time, $\boldsymbol{\tau}$ = 1 ps) was used to regulate the temperature.[88] The total energy of the system was allowed to equilibrate at 300 K, and the data from the last 13 ps of each trajectory were used for further analyses.

Electron localization function: Electron localization function (ELF)[89] for $(AzOH)_2SnI_4$ is computed with the FHI-aims code ("intermediate" numerical defaults, PBE functional, and (4 ×8 × 8) k-point grid).

Data availability

The CIF files associated with this publication have been deposited in the CCDC with deposition numbers 2449501-2449505. These data can be obtained free of charge via www.ccdc.cam.ac.uk/ data_request/cif, or by emailing data_request@ccdc.cam.ac.uk, or by contacting The Cambridge Crystallographic Data Centre, 12 Union Road, Cambridge CB2 1EZ, UK; fax: +44 1223 336033. The atomic positions used in the DFT calculations are listed in the Supplementary Information file. The input and output files for the simulated band structure and spin texture data can be obtained from the Nomad (DOI: 10.17172/NOMAD/2025.12.31-1) database. The spectroscopic data associated with this study can be obtained from Zenodo (DOI: 10.5281/zenodo.19616800). All other data associated with this study are available from the corresponding authors on request.

Acknowledgments

The authors thank Xixi Qin and Peter C. Sercel for helpful discussions. This work was primarily supported as part of the Center for Hybrid Organic–Inorganic Semiconductors for Energy (CHOISE), an Energy Frontier Research Center funded by the Office of Basic Energy Sciences, Office of Science within the U.S. Department of Energy, particularly for synthetic materials, physical characterizations, and part of first-principles calculations. Part of the first-principles band structure calculations was supported by the Duke University Climate Research Innovation Seed Program (CRISP), part of the Duke Climate Commitment. This research used resources of the National Energy Research Scientific Computing Center, a DOE Office of Science User Facility supported by the Office of Science of the U.S. Department of Energy under Contract No. DE-AC02-05CH11231 using NERSC awards BES-ERCAP0024246 and BES-ERCAP0029145. A portion of the research was performed using computational resources sponsored by the Department of Energy's Office of Energy Efficiency and Renewable Energy and located at the National Renewable Energy Laboratory. Part of the work also used Bridges-2 at Pittsburgh Supercomputing Center through allocation CHE240003 from the Advanced Cyberinfrastructure Coordination Ecosystem: Services & Support (ACCESS) program, which is supported by National Science Foundation grants #2138259, #2138286, #2138307, #2137603, and #2138296.

Author Information

Authors and affiliations

Thomas Lord Department of Mechanical Engineering and Materials Science, Duke University, Durham, North Carolina 27708, United States

Rayan Chakraborty, Volker Blum, and David B. Mitzi

Department of Chemistry, Duke University, Durham, North Carolina 27708, United States

Volker Blum and David B. Mitzi

National Laboratory of the Rockies, Golden, Colorado 80401, United States

Yifan Dong, Jacob Shelton, Kelsey Garden, Matthew P. Hautzinger, and Matthew C. Beard

Department of Chemistry, University of Colorado, Boulder, CO 80309, United States

Leo Romanetz

Department of Chemistry, University of California, Riverside, Riverside, California 92507, United States

Yifan Dong

Contributions

R.C. conceived the idea, synthesized the materials, carried out X-ray diffraction measurements and first-principles simulations, and associated analyses; Y.D. and J.L.S. carried out the spin lifetime measurements; L.R. and Y.D. carried out low-temperature UV-Vis measurements; R.C., K.G., and M.P.H. fabricated samples for the spectroscopic measurements; R.C., Y.D., and J.L.S. prepared the manuscript with contributions from D.B.M., M.C.B., V.B., and M.P.H.; M.C.B., D.B.M., V.B., and R.C. acquired funding for the work; D.B.M., V.B., and M.C.B. supervised the project and contributed to the interpretation of the results; All authors read the final version of the manuscript.

Corresponding authors

Correspondence to Matthew C. Beard (matt.beard@nrel.gov) or David B. Mitzi (david.mitzi@duke.edu).

Ethics declarations

The authors declare no competing financial interest.

Supplementary information: Supplementary Tables 1-7, Supplementary Figures 1 – 14, Supplementary Note on the Symmetry Transfer, and Supplementary Data for the geometries used for the DFT calculations.

References

1 Awschalom, D. D. & Flatté, M. E. Challenges for semiconductor spintronics. *Nat. Phys.* **3**, 153-159 (2007). https://doi.org/10.1038/nphys551

2 Schaibley, J. R. *et al.* Valleytronics in 2D materials. *Nat. Rev. Mater.* **1**, 16055 (2016). https://doi.org/10.1038/natrevmats.2016.55

3 Krishnamurthy, S., van Schilfgaarde, M. & Newman, N. Spin lifetimes of electrons injected into GaAs and GaN. *Appl. Phys. Lett.* **83**, 1761-1763 (2003). https://doi.org/10.1063/1.1606873

4 Xu, J. *et al.* How spin relaxes and dephases in bulk halide perovskites. *Nat. Commun.* **15**, 188 (2024). https://doi.org/10.1038/s41467-023-42835-w

5 Wu, M. W., Jiang, J. H. & Weng, M. Q. Spin dynamics in semiconductors. *Phys. Rep.* **493**, 61-236 (2010). https://doi.org/10.1016/j.physrep.2010.04.002

6 Jin, C. *et al.* Imaging of pure spin-valley diffusion current in WS_2-WSe_2 heterostructures. *Science* **360**, 893-896 (2018). https://doi.org/10.1126/science.aao3503

7 Kikkawa, J. M., Smorchkova, I. P., Samarth, N. & Awschalom, D. D. Room-temperature spin memory in two-dimensional electron gases. *Science* **277**, 1284-1287 (1997). https://doi.org/10.1126/science.277.5330.1284

8 Buß, J. H. *et al.* Long room-temperature electron spin lifetimes in highly doped cubic GaN. *Appl. Phys. Lett.* **97** (2010). https://doi.org/10.1063/1.3478838

9 Huang, Y. *et al.* Room-temperature electron spin polarization exceeding 90% in an opto-spintronic semiconductor nanostructure via remote spin filtering. *Nat. Photon.* **15**, 475-482 (2021). https://doi.org/10.1038/s41566-021-00786-y

10 Kikkawa, J. M. & Awschalom, D. D. Resonant spin amplification in n-type GaAs. *Phys. Rev. Lett.* **80**, 4313-4316 (1998). https://doi.org/10.1103/PhysRevLett.80.4313

11 Crooker, S. A. *et al.* Imaging spin transport in lateral ferromagnet/semiconductor structures. *Science* **309**, 2191-2195 (2005). https://doi.org/doi:10.1126/science.1116865

12 Petersen, J., Volz, J. & Rauschenbeutel, A. Nanophotonics. Chiral nanophotonic waveguide interface based on spin-orbit interaction of light. *Science* **346**, 67-71 (2014). https://doi.org/10.1126/science.1257671

13 Wang, J. *et al.* Spin-optoelectronic devices based on hybrid organic-inorganic trihalide perovskites. *Nat. Commun.* **10**, 129 (2019). https://doi.org/10.1038/s41467-018-07952-x

14 Furlan, F. *et al.* Chiral materials and mechanisms for circularly polarized light-emitting diodes. *Nat. Photon.* **18**, 658-668 (2024). https://doi.org/10.1038/s41566-024-01408-z

15 VanOrman, Z. A. *et al.* Chiral light–matter interactions in solution-processable semiconductors. *Nat. Rev. Chem.* **9**, 208-223 (2025). https://doi.org/10.1038/s41570-025-00690-x

16 Suzuki, R. *et al.* Valley-dependent spin polarization in bulk MoS_2 with broken inversion symmetry. *Nat. Nanotechnol.* **9**, 611-617 (2014). https://doi.org/10.1038/nnano.2014.148

17 Zhang, L. *et al.* Room-temperature electrically switchable spin–valley coupling in a van der Waals ferroelectric halide perovskite with persistent spin helix. *Nat. Photon.* **16**, 529-537 (2022). https://doi.org/10.1038/s41566-022-01016-9

18 Zhang, X., Liu, Q., Luo, J.-W., Freeman, A. J. & Zunger, A. Hidden spin polarization in inversion-symmetric bulk crystals. *Nat. Phys.* **10**, 387-393 (2014). https://doi.org/10.1038/nphys2933

19 Xu, X., Yao, W., Xiao, D. & Heinz, T. F. Spin and pseudospins in layered transition metal dichalcogenides. *Nat. Phys.* **10**, 343-350 (2014). https://doi.org/10.1038/nphys2942

20 Liu, Q. *et al.* Search and design of nonmagnetic centrosymmetric layered crystals with large local spin polarization. *Phys. Rev. B* **91**, 235204 (2015). https://doi.org/10.1103/PhysRevB.91.235204

21 Yang, L. *et al.* Long-lived nanosecond spin relaxation and spin coherence of electrons in monolayer MoS_2 and WS_2. *Nat. Phys.* **11**, 830-834 (2015). https://doi.org/10.1038/nphys3419

22 Bertoni, R. *et al.* Generation and Evolution of Spin-, Valley-, and Layer-Polarized Excited Carriers in Inversion-Symmetric WSe_2. *Phys. Rev. Lett.* **117**, 277201 (2016). https://doi.org/10.1103/PhysRevLett.117.277201

23 Yuan, L. *et al.* Uncovering and tailoring hidden Rashba spin-orbit splitting in centrosymmetric crystals. *Nat. Commun.* **10**, 906 (2019). https://doi.org/10.1038/s41467-019-08836-4

24 Brotons-Gisbert, M. *et al.* Spin-layer locking of interlayer excitons trapped in moire potentials. *Nat. Mater.* **19**, 630-636 (2020). https://doi.org/10.1038/s41563-020-0687-7

25 Ashoka, A. *et al.* Local symmetry breaking drives picosecond spin domain formation in polycrystalline halide perovskite films. *Nat. Mater.* **22**, 977-984 (2023). https://doi.org/10.1038/s41563-023-01550-z

26 Arnoldi, B. *et al.* Revealing hidden spin polarization in centrosymmetric van der Waals materials on ultrafast timescales. *Nat. Commun.* **15**, 3573 (2024). https://doi.org/10.1038/s41467-024-47821-4

27 Chakraborty, R. & Mitzi, D. B. Local symmetry breaking and hidden spin polarization in 2D hybrid perovskites with nonprimary ammonium cations. *J. Am. Chem. Soc.* **147**, 30545-30573 (2025). https://doi.org/10.1021/jacs.5c05250

28 Kim, Y. H. *et al.* Chiral-induced spin selectivity enables a room-temperature spin light-emitting diode. *Science* **371**, 1129-1133 (2021). https://doi.org/10.1126/science.abf5291

29 Crassous, J. *et al.* Materials for chiral light control. *Nat. Rev. Mater.* **8**, 365-371 (2023). https://doi.org/10.1038/s41578-023-00543-3

30 Dryzhakov, B. *et al.* Spin switchable optical phenomena in Rashba band structures through intersystem crossing in momentum space in solution-processing 2D-superlattice perovskite film. *Nat. Commun.* **16**, 4247 (2025). https://doi.org/10.1038/s41467-025-57834-2

31 Briscoe, J. & Shi, J. Photogalvanic effects in non-centrosymmetric halide perovskites. *Nat. Rev. Phys.* **7**, 270-279 (2025). https://doi.org/10.1038/s42254-025-00822-8

32 Yang, S., Vetter, E., Wang, T., Amassian, A. & Sun, D. Observation of long spin lifetime in $MAPbBr_3$ single crystals at room temperature. *J. Phys. Mater.* **3**, 015012 (2020). https://doi.org/10.1088/2515-7639/ab69b0

33 Wang, M. *et al.* Extremely Long Spin Lifetime of Light-Emitting States in Quasi-2D Perovskites through Orbit-Orbit Interaction. *J. Phys. Chem. Lett.* **11**, 3647-3652 (2020). https://doi.org/10.1021/acs.jpclett.0c00842

34 Huang, Y. *et al.* Quantification of chirality induced spin-orbit coupling for long spin polarized lifetime in hybrid perovskite. *J. Phys. Chem. Lett.* **16**, 2378-2384 (2025). https://doi.org/10.1021/acs.jpclett.5c00119

35 McKechnie, S. *et al.* Dynamic symmetry breaking and spin splitting in metal halide perovskites. *Phys. Rev. B* **98**, 085108 (2018). https://doi.org/10.1103/PhysRevB.98.085108

36 Kirstein, E. *et al.* Coherent spin dynamics of electrons in two-dimensional $(PEA)_2PbI_4$ perovskites. *Nano Lett.* **23**, 205-212 (2023). https://doi.org/10.1021/acs.nanolett.2c03975

37 Mihalyi-Koch, W. *et al.* Revealing hidden non-centrosymmetry in globally centrosymmetric 2D halide perovskites. *Chem* **10**, 2180-2195 (2024). https://doi.org/10.1016/j.chempr.2024.03.012

38 Saparov, B. & Mitzi, D. B. Organic-inorganic perovskites: structural versatility for functional materials design. *Chem. Rev.* **116**, 4558-4596 (2016). https://doi.org/10.1021/acs.chemrev.5b00715

39 Gao, Y. *et al.* Molecular engineering of organic-inorganic hybrid perovskites quantum wells. *Nat. Chem.* **11**, 1151-1157 (2019). https://doi.org/10.1038/s41557-019-0354-2

40 Jana, M. K. *et al.* Organic-to-inorganic structural chirality transfer in a 2D hybrid perovskite and impact on Rashba-Dresselhaus spin-orbit coupling. *Nat. Commun.* **11**, 4699 (2020). https://doi.org/10.1038/s41467-020-18485-7

41 Malinowski, A. *et al.* Spin relaxation in $GaAs/Al_xGa_{1-x}As$ quantum wells. *Phys. Rev. B* **62**, 13034-13039 (2000). https://doi.org/10.1103/PhysRevB.62.13034

42 Litvinenko, K. L. *et al.* Spin lifetime in high quality InSb epitaxial layers grown on GaAs. *J. Appl. Phys.* **101** (2007). https://doi.org/10.1063/1.2719017

43 Zhou, M., Sarmiento, J. S., Fei, C., Zhang, X. & Wang, H. Effect of composition on the spin relaxation of lead halide perovskites. *J. Phys. Chem. Lett.* **11**, 1502-1507 (2020). https://doi.org/10.1021/acs.jpclett.0c00004

44 Chakraborty, R. *et al.* Rational design of non-centrosymmetric hybrid halide perovskites. *J. Am. Chem. Soc.* **145**, 1378-1388 (2023). https://doi.org/10.1021/jacs.2c12034

45 Chakraborty, R., Sercel, P. C., Qin, X., Mitzi, D. B. & Blum, V. Design of two-dimensional hybrid perovskites with giant spin splitting and persistent spin textures. *J. Am. Chem. Soc.* **146**, 34811-34821 (2024). https://doi.org/10.1021/jacs.4c13597

46 Chakraborty, R. & Nag, A. Correlation of dielectric confinement and excitonic binding energy in 2D layered hybrid perovskites using temperature dependent photoluminescence. *J. Phys. Chem. C* **124**, 16177-16185 (2020). https://doi.org/10.1021/acs.jpcc.0c04284

47 Chen, X. *et al.* Tuning spin-polarized lifetime in two-dimensional metal-halide perovskite through exciton binding energy. *J. Am. Chem. Soc.* **143**, 19438-19445 (2021). https://doi.org/10.1021/jacs.1c08514

48 Gotoh, H. *et al.* Effect of electron–hole interaction on electron spin relaxation in GaAs/AlGaAs quantum wells at room temperature. *J. Appl. Phys.* **87**, 3394-3398 (2000). https://doi.org/10.1063/1.372356

49 Jana, M. K. *et al.* Structural descriptor for enhanced spin-splitting in 2D hybrid perovskites. *Nat. Commun.* **12**, 4982 (2021). https://doi.org/10.1038/s41467-021-25149-7

50 Knutson, J. L., Martin, J. D. & Mitzi, D. B. Tuning the band gap in hybrid tin iodide perovskite semiconductors using structural templating. *Inorg. Chem.* **44**, 4699-4705 (2005). https://doi.org/10.1021/ic050244q

51 Blum, V. *et al.* Ab initio molecular simulations with numeric atom-centered orbitals. *Computer Physics Communications* **180**, 2175-2196 (2009). https://doi.org/10.1016/j.cpc.2009.06.022

52 Togo, A. First-principles Phonon Calculations with Phonopy and Phono3py. *J. Phys. Soc. Jpn.* **92**, 012001 (2022). https://doi.org/10.7566/JPSJ.92.012001

53 Zhai, Y. *et al.* Giant Rashba splitting in 2D organic-inorganic halide perovskites measured by transient spectroscopies. *Sci. Adv.* **3**, e1700704 (2017). https://doi.org/doi:10.1126/sciadv.1700704

54 Ishizaka, K. *et al.* Giant Rashba-type spin splitting in bulk BiTeI. *Nat. Mater.* **10**, 521-526 (2011). https://doi.org/10.1038/nmat3051

55 Zhao, H. J. *et al.* Large spin splittings due to the orbital degree of freedom and spin textures in a ferroelectric nitride perovskite. *Phys. Rev. B* **102**, 041203 (2020). https://doi.org/10.1103/PhysRevB.102.041203

56 Liu, Q., Guo, Y. & Freeman, A. J. Tunable Rashba effect in two-dimensional $LaOBiS_2$ films: ultrathin candidates for spin field effect transistors. *Nano Lett.* **13**, 5264-5270 (2013). https://doi.org/10.1021/nl4027346

57 Walser, M. P., Reichl, C., Wegscheider, W. & Salis, G. Direct mapping of the formation of a persistent spin helix. *Nat. Phys.* **8**, 757-762 (2012). https://doi.org/10.1038/nphys2383

58 Hong, X., Ishihara, T. & Nurmikko, A. V. Dielectric confinement effect on excitons in PbI4-based layered semiconductors. *Phys. Rev. B Condens. Matter* **45**, 6961-6964 (1992). https://doi.org/10.1103/physrevb.45.6961

59 Cheng, B. *et al.* Extremely reduced dielectric confinement in two-dimensional hybrid perovskites with large polar organics. *Commun. Phys.* **1** (2018). https://doi.org/10.1038/s42005-018-0082-8

60 Katan, C., Mercier, N. & Even, J. Quantum and dielectric confinement effects in lower-dimensional hybrid perovskite semiconductors. *Chem. Rev.* **119**, 3140-3192 (2019). https://doi.org/10.1021/acs.chemrev.8b00417

61 Yin, J. *et al.* Tuning hot carrier cooling dynamics by dielectric confinement in two-dimensional hybrid perovskite crystals. *ACS Nano* **13**, 12621-12629 (2019). https://doi.org/10.1021/acsnano.9b04085

62 Korn, T. Time-resolved studies of electron and hole spin dynamics in modulation-doped GaAs/AlGaAs quantum wells. *Phys. Rep.* **494**, 415-445 (2010). https://doi.org/https://doi.org/10.1016/j.physrep.2010.05.001

63 Giovanni, D. *et al.* Highly spin-polarized carrier dynamics and ultralarge photoinduced magnetization in $CH_3NH_3PbI_3$ perovskite thin films. *Nano Lett.* **15**, 1553-1558 (2015). https://doi.org/10.1021/nl5039314

64 Yang, C., Cui, X., Shen, S.-Q., Xu, Z. & Ge, W. Spin relaxation in submonolayer and monolayer InAs structures grown in a GaAs matrix. *Phys. Rev. B* **80**, 035313 (2009). https://doi.org/10.1103/PhysRevB.80.035313

65 Mai, C. *et al.* Many-body effects in valleytronics: direct measurement of valley lifetimes in single-layer MoS_2. *Nano Lett.* **14**, 202-206 (2014). https://doi.org/10.1021/nl403742j

66 Fang, M. *et al.* Recent advances in tunable spin–orbit coupling using ferroelectricity. *APL Mater.* **9** (2021). https://doi.org/10.1063/5.0052553

67 Sohn, J., Lee, J. M. & Lee, H. W. Dyakonov-Perel-like orbital and spin relaxations in centrosymmetric systems. *Phys. Rev. Lett.* **132**, 246301 (2024). https://doi.org/10.1103/PhysRevLett.132.246301

68 Zhang, D. *et al.* Room temperature near unity spin polarization in 2D Van der Waals heterostructures. *Nat. Commun.* **11**, 4442 (2020). https://doi.org/10.1038/s41467-020-18307-w

69 Leyland, W. J. H. *et al.* Enhanced spin-relaxation time due to electron-electron scattering in semiconductor quantum wells. *Phys. Rev. B* **75**, 165309 (2007). https://doi.org/10.1103/PhysRevB.75.165309

70 Wang, Q. *et al.* Room-Temperature nanoseconds spin relaxation in WTe_2 and $MoTe_2$ Thin Films. *Adv. Sci.* **5**, 1700912 (2018). https://doi.org/10.1002/advs.201700912

71 Xu, R., Zhang, Z., Liang, J. & Zhu, H. Valleytronics: fundamental challenges and materials beyond transition metal chalcogenides. *Small* **21**, 2402139 (2025). https://doi.org/https://doi.org/10.1002/smll.202402139

72 Riley, J. M. *et al.* Direct observation of spin-polarized bulk bands in an inversion-symmetric semiconductor. *Nat. Phys.* **10**, 835-839 (2014). https://doi.org/10.1038/nphys3105

73 Li, X., Hoffman, J. M. & Kanatzidis, M. G. The 2D halide perovskite rulebook: how the spacer influences everything from the structure to optoelectronic device efficiency. *Chem. Rev.* **121**, 2230-2291 (2021). https://doi.org/10.1021/acs.chemrev.0c01006

74 Chen, J. *et al.* Intermolecular forces regulating the phase-transition temperatures in organic–inorganic hybrid materials. *Inorg. Chem.* **63**, 7770-7779 (2024). https://doi.org/10.1021/acs.inorgchem.4c00177

75 Gajhede, M., Anthoni, U., Christophersen, C. & Nielsen, P. H. Hydrogen bonding in 3-azetidinol. I. Crystal and molecular structure. *Acta Crystallogr. B* **45**, 562-566 (1989). https://doi.org/doi:10.1107/S0108768189006476

76 Dill, R. D. *et al.* Near-infrared absorption features of triplet-pair states assigned by photoinduced-absorption-detected magnetic resonance. *J. Phys. Chem. Lett.* **14**, 2387-2394 (2023). https://doi.org/10.1021/acs.jpclett.2c03665

77 Changenet, P. & Hache, F. Artifact-free balanced detection for the measurement of circular dichroism with a sub-picosecond time resolution. *Opt. Express* **31**, 21296-21310 (2023). https://doi.org/10.1364/OE.489468

78 Levchenko, S. V. *et al.* Hybrid functionals for large periodic systems in an all-electron, numeric atom-centered basis framework. *Comp. Phys. Commun.* **192**, 60-69 (2015). https://doi.org/https://doi.org/10.1016/j.cpc.2015.02.021

79 Huhn, W. P. & Blum, V. One-hundred-three compound band-structure benchmark of post-self-consistent spin-orbit coupling treatments in density functional theory. *Phys. Rev. Mater.* **1**, 033803 (2017). https://doi.org/10.1103/PhysRevMaterials.1.033803

80 Mercier, N., Poiroux, S., Riou, A. & Batail, P. Unique hydrogen bonding correlating with a reduced band gap and phase transition in the hybrid perovskites $(HO(CH_2)_2NH_3)_2PbX_4$ (X = I, Br). *Inorg. Chem.* **43**, 8361-8366 (2004). https://doi.org/10.1021/ic048814u

81 Perdew, J. P., Burke, K. & Ernzerhof, M. Generalized gradient approximation made simple. *Phys. Rev. Lett.* **77**, 3865-3868 (1996). https://doi.org/10.1103/PhysRevLett.77.3865

82 Tkatchenko, A. & Scheffler, M. Accurate molecular van der Waals interactions from ground-state electron density and free-atom reference data. *Phys. Rev. Lett.* **102**, 073005 (2009). https://doi.org/10.1103/PhysRevLett.102.073005

83 Heyd, J., Scuseria, G. E. & Ernzerhof, M. Hybrid functionals based on a screened Coulomb potential. *J. Chem. Phys.* **118**, 8207-8215 (2003). https://doi.org/10.1063/1.1564060

84 Heyd, J., Scuseria, G. E. & Ernzerhof, M. Erratum: “Hybrid functionals based on a screened Coulomb potential” [J. Chem. Phys. 118, 8207 (2003)]. *J. Chem. Phys.* **124**, 219906 (2006). https://doi.org/10.1063/1.2204597

85 Krukau, A. V., Vydrov, O. A., Izmaylov, A. F. & Scuseria, G. E. Influence of the exchange screening parameter on the performance of screened hybrid functionals. *J. Chem. Phys.* **125**, 224106 (2006). https://doi.org/10.1063/1.2404663

86 Zhao, R. *et al.* Quasi-four-component method with numeric atom-centered orbitals for relativistic density functional simulations of molecules and solids. *Phys. Rev. B* **103**, 245144 (2021). https://doi.org/10.1103/PhysRevB.103.245144

87 Togo, A. & Tanaka, I. First principles phonon calculations in materials science. *Scr. Mater.* **108**, 1-5 (2015). https://doi.org/https://doi.org/10.1016/j.scriptamat.2015.07.021

88 Bussi, G., Donadio, D. & Parrinello, M. Canonical sampling through velocity rescaling. *J. Chem. Phys.* **126**, 014101 (2007). https://doi.org/10.1063/1.2408420

89 Savin, A., Nesper, R., Wengert, S. & Fässler, T. F. ELF: The Electron Localization Function. *Angew. Chem. Int. Ed.* **36**, 1808-1832 (1997). https://doi.org/https://doi.org/10.1002/anie.199718081

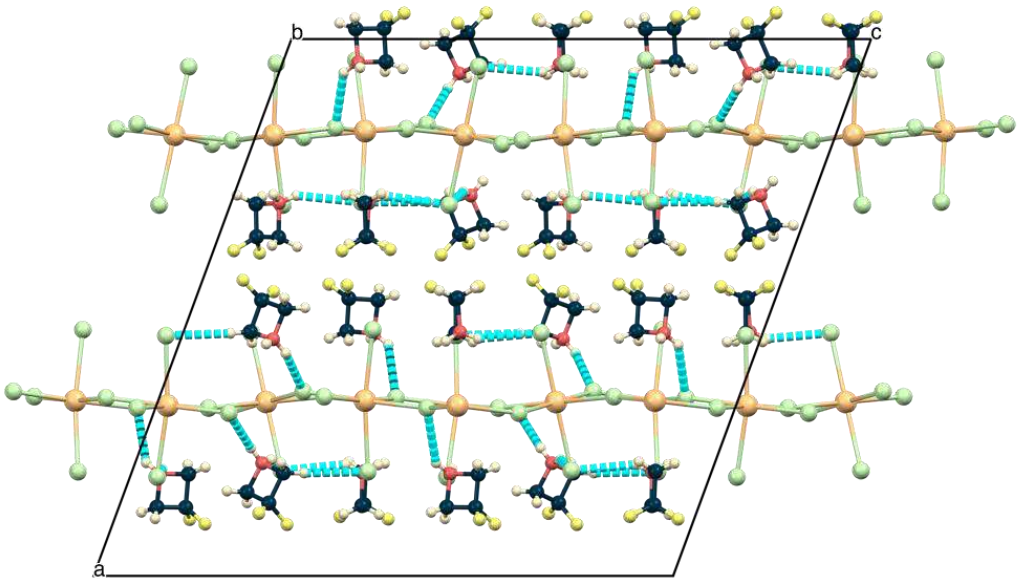
Extended data.

Extended Data Table 1. Spin splitting energies from first-principles DFT calculations with hybrid HSE06 functional and spin-orbit coupling.
Γ – Y and Γ – Z correspond to directions in the reciprocal (*k*) space that are parallel to the metal halide layers in the crystal structures.

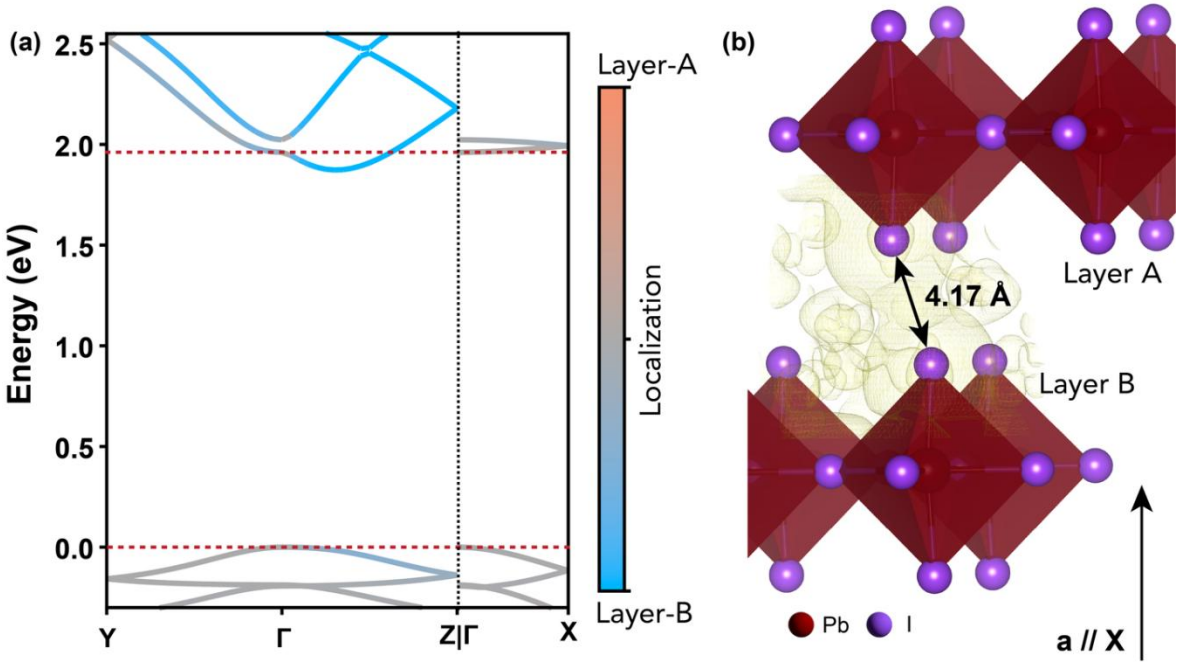
Composition	Band edge	k-path direction	Spin-splitting energy (meV)
$(AzOH)_2PbI_4$	valence	Γ - Y	187.4
		Γ - Z	187.7
	conduction	Γ - Y	62.1
		Γ - Z	433.6
$(AzOH)_2SnI_4$	valence	Γ - Y	190.0
		Γ - Z	190.0
	conduction	Γ - Y	9.5
		Γ - Z	237.4
$(AzF_2)_2PbI_4$	valence	Γ - Y	0.5
		Γ - Z	0.0
	conduction	Γ - Y	13.8
		Γ - Z	0.1

Extended Data Table 2. Spin half-lifetimes at room temperature, estimated in this work.
For consistency, a bi-exponential model was used to fit the signal decay, where $\boldsymbol{\tau}_1$ and $\boldsymbol{\tau}_2$ represent the half lifetime components; corresponding $\boldsymbol{\tau}_s$ (i.e., spin lifetime; as included in Table 1) refers to 2 $\boldsymbol{\tau}_2$. For $(AzOH)_2SnI_4$, superscripts [1] and [2] refer to measurements with left and right circularly polarized excitation (pump), respectively.

2DHPs	Thin film/single crystal	$\boldsymbol{\tau_1}$	$\boldsymbol{\tau_2}$
$(AzOH)_2PbI_4$	Single crystal	1.3 ps (46%)	270.0 ps (54%)
$(AzOH)_2PbI_4$	Thin film	8.1 ps (47%)	343.0 ps (53%)
$(AzOH)_2SnI_4$	Thin film	52.1 ps (74%)[1]	2.3 ns (26%)[1]
		46.3 ps (74%)[2]	2.4 ns (26%)[2]
$(AzF_2)_2PbI_4$	Thin film	0.6 ps (53%)	3.5 ps (47%)
$(EOA)_2PbI_4$	Thin film	1.4 ps (81%)	15.0 ps (20%)

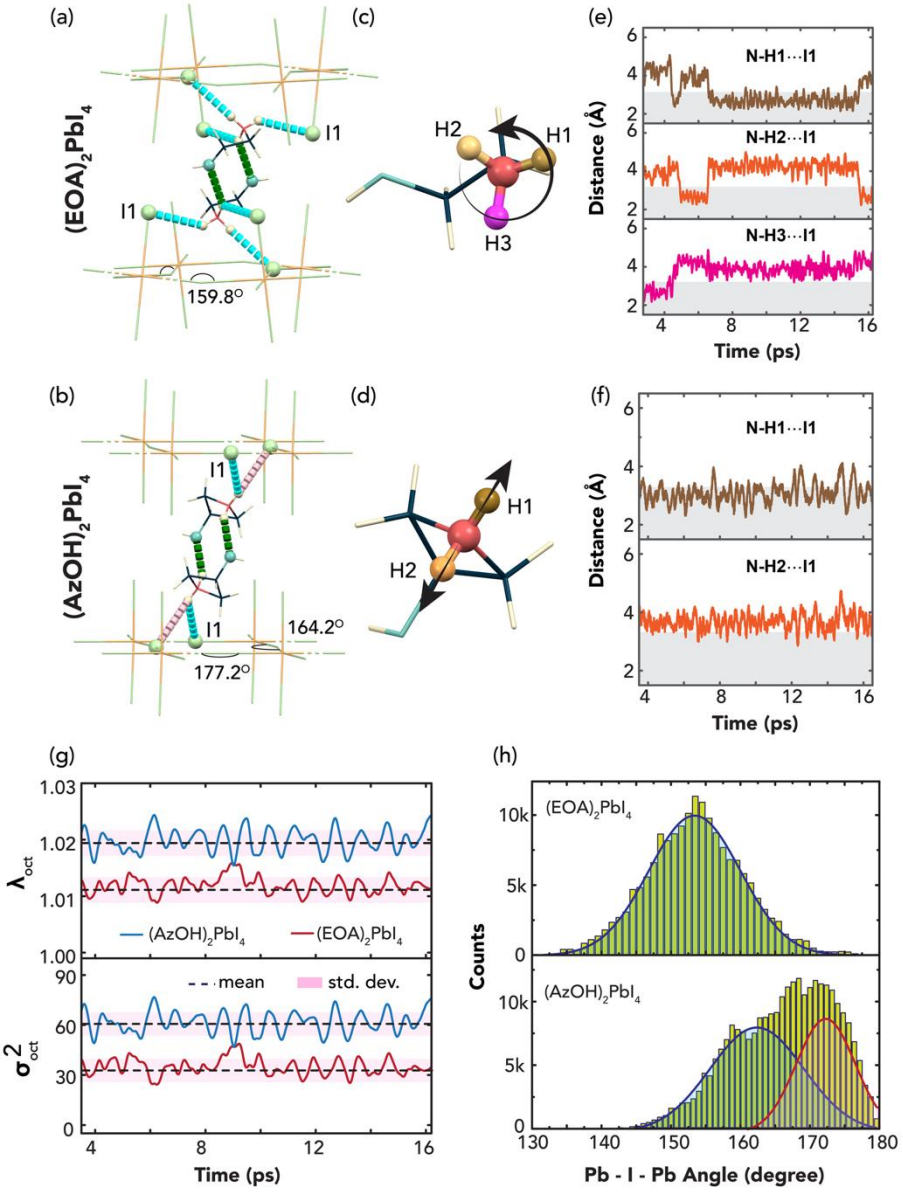


Extended Data Figure 1. Crystal structure of $(AzF_2)_2PbI_4$ at room temperature.
The blue dashed lines indicate N – H ⋯ I interactions. The following colors are used for different atoms: orange (lead; Pb), green (iodine; I), red (nitrogen; N), black (carbon; C), gray (hydrogen; H), and light yellow (fluorine; F).



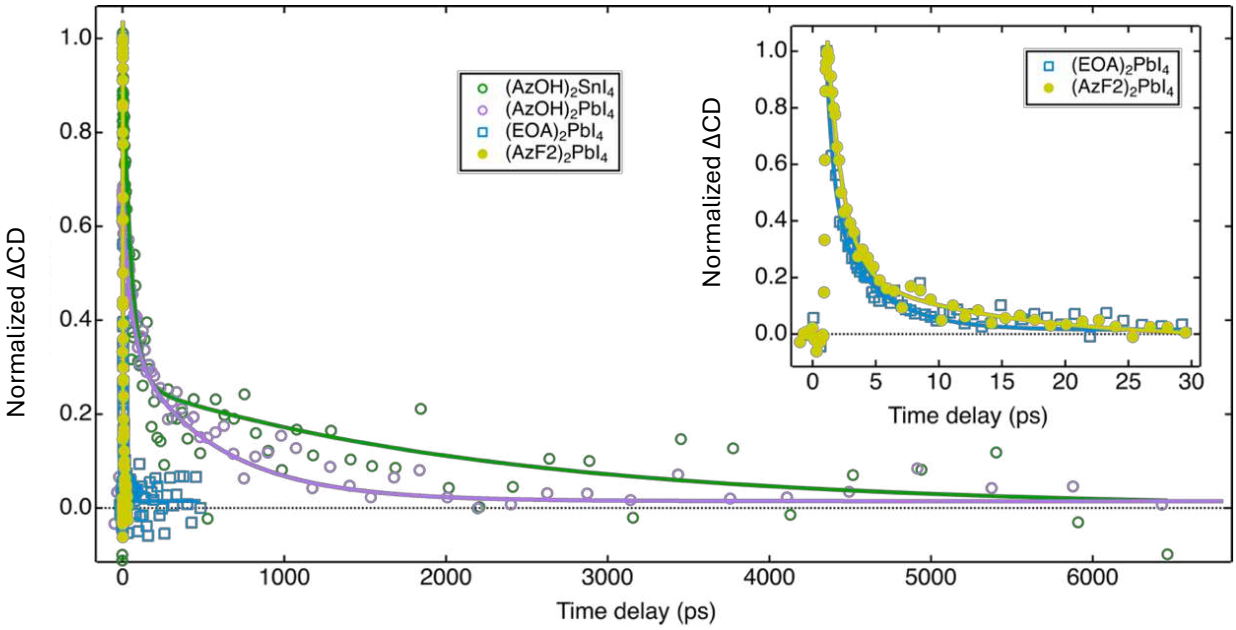
Extended Data Figure 2. Layer-dependent localization of electronic states in $(AzOH)_2PbI_4$.
(a) Comparison of localization of the DFT (HSE06 + SOC)-derived six exemplary electronic bands and at the band edges in $(AzOH)_2PbI_4$ along the Y– Γ – Z and Γ – X directions, calculated using

Mulliken analysis, following the method described in reference[45]; the red dashed lines indicate the extrema along the Γ – X direction, which also correspond to the out-of-plane direction (interlayer) in real space; (b) plot of electron density difference (yellow shaded regions; calculated with DFT) compared to free atom densities in the interlayer region in $(AzOH)_2PbI_4$; the organic cations have been removed from the displayed image for clarity.



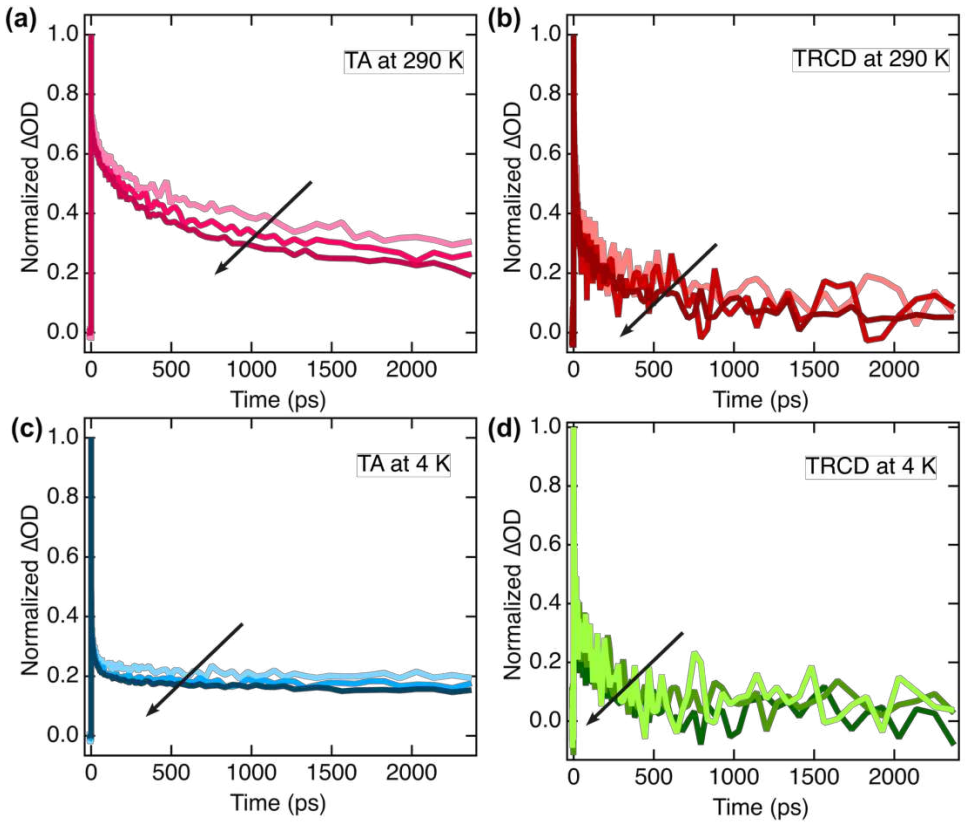
Extended Data Figure 3. Organic-to-inorganic symmetry transfer in A_2PbI_4 perovskites with A = 2-hydroxyethylammonium (EOA) and 3-hydroxyazetidinium (AzOH).
Noncovalent N–H···I (blue or red dashed lines for shorter and longer distances than 3.0 Å, respectively), and N–H···O (green dashed lines) in (a) $(EOA)_2PbI_4$ and (b) $(AzOH)_2PbI_4$ crystals at room temperature. Schematics show dynamics involving the ammonium group in (c) EOA and (d) AzOH cations in the hybrid structures; dynamics of (e, f) N-H···I interactions (with respect to

iodine labeled as I1 in a, b, and hydrogens labeled in c, d; the shaded regions mark the cut-off applied to define hydrogen bonding interactions); (g) octahedral distortion parameters (averaged over 0.75 ps), and (h) distribution of Pb – I – Pb angles (the red and blue curves correspond to Gaussian fitting functions); data for c – h are simulated using AIMD at constant volume and temperature (T = 300 K); see Supporting Note in SI for extended discussion and definitions of the distortion parameters; briefly, the dynamics indicate periodic switching of N-H···I interactions in $(EOA)_2PbI_4$ through stepwise rotation of the C – N bond; however, such rotation is restricted in $(AzOH)_2PbI_4$ due to the additional C – N linkage on the ammonium group; the above restriction ultimately leads to asymmetric N-H···I interactions, dynamically preserved larger octahedral distortions, and inversion symmetry breaking of the Pb – I layers in $(AzOH)_2PbI_4$.

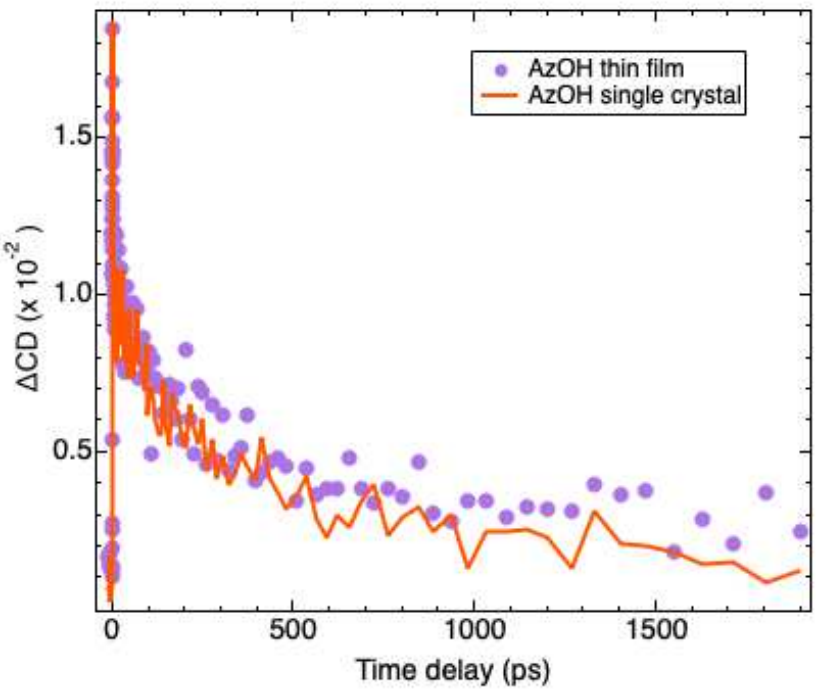


Extended Data Figure 4. Normalized TRCD kinetics for spin lifetimes measured at 290 K on 2DHP films.

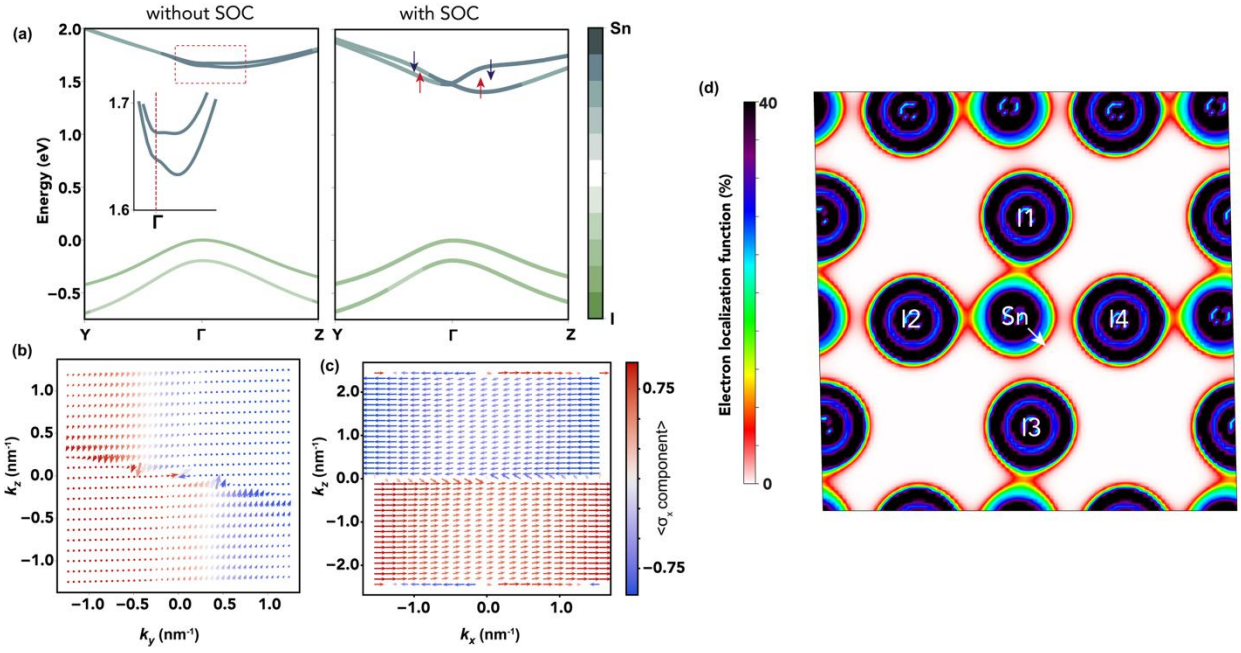
The inset shows a shorter time window of up to 30 ps for $(EOA)_2PbI_4$ and $(AzF_2)_2PbI_4$.



Extended Data Figure 5. Fluence-dependence of TA and TRCD dynamics of $(AzOH)_2PbI_4$. (a, c) TA and (b, d) TRCD response of $(AzOH)_2PbI_4$ films at 290 K (a, b) and 4 K (c, d) exhibit minor dependence on the pump fluence; the arrow indicates an increase in the pump fluence.

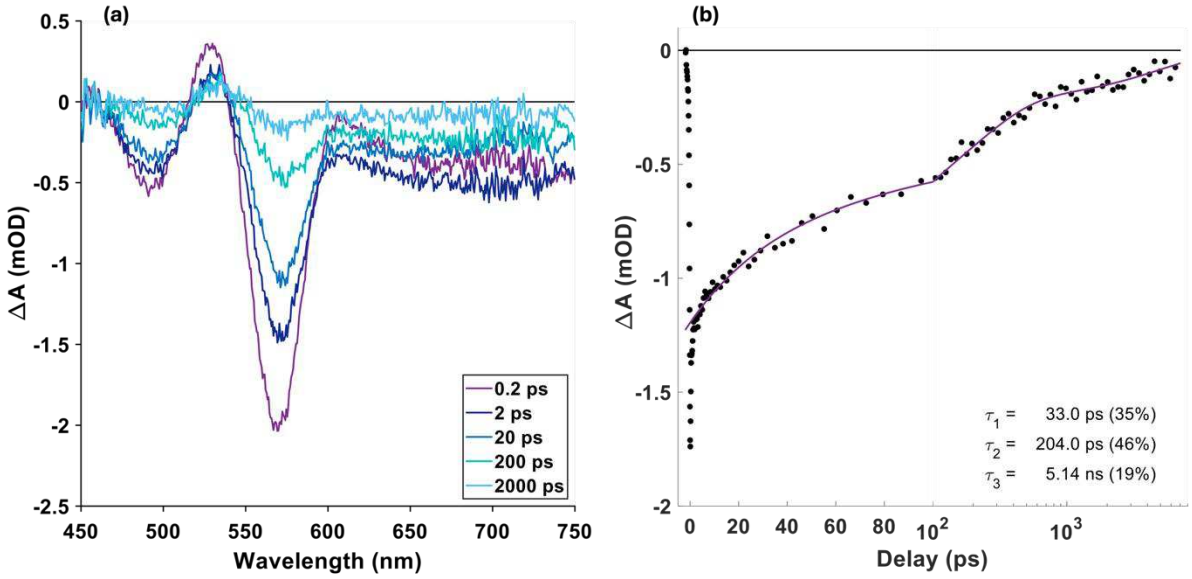


Extended Data Figure 6. Comparison of spin dynamics (TRCD response) of $(AzOH)_2PbI_4$ between single crystal and thin film.



Extended Data Figure 7. Structural origin of spin valleys in $(AzOH)_2SnI_4$.
(a) DFT-derived (HSE06, without SOC) electronic band structure for the valence and conduction band edges (area enclosed in the red dashed rectangle is shown in the inset); red and blue arrows indicate spin polarizations for a layer-localized set of bands, as obtained from spin texture calculations using DFT (PBE+SOC); two-dimensional spin texture plot of $(AzOH)_2SnI_4$ for the

conduction band minima on the (b) k_y-k_z (parallel to the Sn – I layer), and (c) k_x-k_z (orthogonal to the Sn – I layer) planes, simulated with DFT (PBE + SOC); plot of the electron localization function (ELF; PBE, without SOC; see Methods) on the *(010)* plane of $(AzOH)_2SnI_4$; the different shapes of the low-ELF regions surrounding Sn (iodine-derived ELFs are marked as I1, I2, I3, and I4; the arrow highlights distortion direction for the Sn-derived ELF) are consequences of the polar distortions and inversion symmetry breaking.



Extended Data Figure 8. Transient absorption response of $(AzOH)_2SnI_4$ film at 290 K. The dynamics are plotted as functions of (a) wavelength at five representative delay times, and (b) delay time (the numbers in the inset correspond to half lifetime components obtained from the exponential decay function).

Supplementary Files

This is a list of supplementary files associated with this preprint. Click to download.

- AzXspinlifetimeSIrevised2clean.pdf